JM PAPERS

Fingering convection in a spherical shell

Théo Tassin[1], Thomas Gastine[1],† and Alexandre Fournier[1]

[1]Université Paris Cité, Institut de physique du globe de Paris, CNRS, F-75005 Paris, France

We use 123 three-dimensional direct numerical simulations to study fingering convection in non-rotating spherical shells. We investigate the scaling behaviour of the flow length scale, the non-dimensional heat and compositional fluxes *Nu* and *Sh* and the mean convective velocity over the fingering convection instability domain defined by $1 \leq R_\rho < Le$, R_ρ being the ratio of density perturbations of thermal and compositional origins and *Le* the Lewis number. We show that the chemical boundary layers are marginally unstable and adhere to the laminar Prandtl–Blasius model, hence explaining the asymmetry between the inner and outer spherical shell boundary layers. We develop scaling laws for two asymptotic regimes close to the two edges of the instability domain, namely $R_\rho \lesssim Le$ and $R_\rho \gtrsim 1$. For the former, we develop novel power laws of a small parameter ϵ measuring the distance to onset, which differ from theoretical laws published to date in Cartesian geometry. For the latter, we find that the Sherwood number *Sh* gradually approaches a scaling $Sh \sim Ra_\xi^{1/3}$ when $Ra_\xi \gg 1$; and that the Péclet number accordingly follows $Pe \sim Ra_\xi^{2/3}|Ra_T|^{-1/4}$, Ra_T and Ra_ξ being the thermal and chemical Rayleigh numbers. When the Reynolds number exceeds a few tens, we report on a secondary instability which takes the form of large-scale toroidal jets which span the entire spherical domain. Jets distort the fingers, resulting in Reynolds stress correlations, which in turn feed the jet growth until saturation. This nonlinear phenomenon can yield relaxation oscillation cycles.

Key words: double diffusive convection, jets

1. Introduction

Double-diffusive effects are ubiquitous in fluid envelopes of planetary interiors. For instance, in the liquid iron core of terrestrial planets, the convective motions are driven by thermal and compositional perturbations which originate from the secular cooling and the inner-core growth (e.g. Roberts & King 2013). Several internal evolution models coupled with *ab initio* computations and high-pressure experiments for core conductivity are suggestive of a thermally stratified layer underneath the core–mantle boundaries of

Mercury (Hauck *et al.* 2004) and the Earth (e.g. Pozzo *et al.* 2012; Ohta *et al.* 2016). Such a fluid layer could harbour fingering convection, where thermal stratification is stable whilst compositional stratification is unstable (Stern 1960). In contrast, in the deep interior of the gas giants Jupiter and Saturn, the internal models by Mankovich & Fortney (2020) suggest the presence of a stabilising helium gradient opposed to the destabilising thermal stratification, a physical configuration prone to semi-convective instabilities (Veronis 1965).

The linear stability analysis of double-diffusive systems, as carried out by e.g. Stern (1960), Veronis (1965) and Baines & Gill (1969), shows that fingering convection occurs in planar geometry when the density ratio $R_\rho = |\alpha_T \Delta T|/\alpha_\xi \Delta \xi$ belongs to the interval

$$1 \leq R_\rho < Le, \tag{1.1}$$

where α_T (α_ξ) are the thermal (compositional) expansion coefficient and ΔT ($\Delta \xi$) are the perturbations of thermal (compositional) origin. In the above expression, Le is the Lewis number, defined by the ratio of the thermal and solutal diffusivities. Note that the upper bound of the instability domain, Le, ignores a correcting term that is a function of the structure of the unstable mode, and that becomes negligible in the limit of large thermal and compositional Rayleigh numbers, to be defined below (see e.g. Turner 1973, § 8.1.2). Close to onset, the instability takes the form of vertically elongated fingers, whose typical horizontal size $\mathcal{L}_h$ results from a balance between buoyancy and viscosity and follows $\mathcal{L}_h = |Ra_T|^{-1/4} d$, where Ra_T is the thermal Rayleigh number and d is the vertical extent of the fluid domain (e.g. Schmitt 1979*b*; Taylor & Bucens 1989; Smyth & Kimura 2007). Developed salt fingers frequently give rise to secondary instabilities, such as the collective instability (Stern 1969), thermohaline staircase formation (Radko 2003) or jets (Holyer 1984). The saturated state of the instability is therefore frequently made up of a mixture of small-scale fingers and large-scale structures commensurate with the size of the fluid domain. A mean-field formalism can then be successfully employed to describe the secondary instabilities (e.g. Traxler *et al.* 2011*b*; Radko 2013).

Following Radko & Smith (2012), Brown, Garaud & Stellmach (2013) hypothesise that fingering convection saturates once the growth rate of the secondary instability is comparable to that of the primary fingers. In the context of the low Prandtl numbers ($Pr \ll 1$) relevant to stellar interiors, they derive three branches of semi-analytical scaling laws for the transport of heat and chemical composition which depend on the value of $r_\rho = (R_\rho - 1)/(Le - 1)$. These theoretical scaling laws accurately account for the behaviours observed in local three-dimensional (3-D) numerical simulations (see, e.g. Garaud 2018, figure 2). In the context of large Prandtl numbers, Radko (2010) developed a weakly nonlinear model for salt fingers which predicts that the scaling behaviours for the transport of heat and chemical composition should follow power laws of the distance to onset (see also Stern & Radko 1998; Radko & Stern 2000; Xie *et al.* 2017).

Besides the growth of the celebrated thermohaline staircases (Garaud *et al.* 2015), the fingering instability can also lead to the formation of large-scale horizontal flows or jets. By applying the methods of Floquet theory, Holyer (1984) demonstrated that a non-oscillatory secondary instability could actually grow faster than the collective instability for fluids with $Pr \gtrsim 1$. This instability takes the form of a mean horizontally invariant flow which distorts the fingers (see her figure 1). Cartesian numerical simulations in two dimensions carried out by Shen (1995) later revealed that the nonlinear evolution of this instability yields a strong shear that eventually disrupts the vertical coherence of the fingers (see his figure 2). Jets were also obtained in the two-dimensional (2-D) simulations by Radko (2010) for configurations with $Pr = 10^{-2}$ and $Le = 3$ and by

Garaud & Brummell ([2015](#)) for $Pr = 0.03$ and $Le \approx 33.3$. In addition to the direct numerical simulations, jets have also been observed in single-mode truncated models by Paparella & Spiegel ([1999](#)) and Liu, Julien & Knobloch ([2022](#)). The qualitative description of the instability developed by Stern & Simeonov ([2005](#)) underlines the analogy with tilting instabilities observed in Rayleigh–Bénard convection (e.g. Goluskin *et al.* [2014](#)): jets shear apart fingers, which in turn feed the growth of jets via Reynolds stress correlations. The nonlinear saturation of the instability can occur via the disruption of the fingers (Shen [1995](#)), but can also yield relaxation oscillations with a predator–prey-like behaviour between jets and fingers (Garaud & Brummell [2015](#); Xie, Julien & Knobloch [2019](#)). Garaud & Brummell ([2015](#)) suggest, however, that this instability may be confined to 2-D fluid domains, and hence question the relevance of jet formation in three dimensions when $Pr \ll 1$. The 3-D bounded planar models by Yang, Verzicco & Lohse ([2016](#)) for $Pr = 7$, however, exhibit jets for simulations with $R_\rho = 1.6$. This raises the question of the physical phenomena which govern the instability domain of jets. In addition, to date, jets have only been observed in local simulations containing a few tens of fingers; their relevance in 3-D global domains therefore remains to be assessed.

The vast majority of the theoretical and numerical models discussed above adopt a local Cartesian approach. Two configurations are then considered. The most common, termed unbounded, resorts to using a triply periodic domain without boundary layers (e.g. Stellmach *et al.* [2011](#); Brown *et al.* [2013](#)). Conversely, in the bounded configurations, the flow is maintained between two horizontal plates and boundary layers can form in the vicinity of the boundaries (e.g. Schmitt [1979*b*](#); Radko & Stern [2000](#); Yang *et al.* [2015](#)). This latter configuration is also relevant to laboratory experiments in which thermal and/or chemical compositions are imposed at the boundaries of the fluid domain (e.g. Taylor & Bucens [1989](#); Hage & Tilgner [2010](#); Rosenthal, Lüdemann & Tilgner [2022](#)). One of the key issues of the bounded configuration is to express scaling laws that depend on the thermal ΔT and/or compositional $\Delta \xi$ contrasts imposed over the layer. Early experiments by Turner ([1967](#)) and Schmitt ([1979*a*](#)) suggest that the salinity flux grossly follows a 4/3 power law on $\Delta \xi$, with an additional secondary dependence on R_ρ, Pr and Le (see Taylor & Veronis [1996](#)). Expressed in dimensionless quantities, this translates to $Sh \sim Ra_\xi^{1/3}$, Sh being the Sherwood number and Ra_ξ a composition-based Rayleigh number. This is the double-diffusive counterpart of the classical heat transport model for turbulent convection in which the heat flux is assumed to be depth independent (Priestley [1954](#)). Yang *et al.* ([2015](#)) refined this scaling by extending the Grossmann–Lohse theory for classical Rayleigh–Bénard convection (hereafter GL, see Grossmann & Lohse [2000](#)) to the fingering configuration. Considering a suite of 3-D bounded Cartesian numerical simulations with $Pr = 7$ and $Le = 100$, Yang *et al.* ([2016](#)) then found that the dependence of Sh upon Ra_ξ is well accounted for by the GL theory. Scaling laws for the Reynolds number Re put forward by Yang *et al.* ([2016](#)) involve an extra dependence on the density ratio with an empirical exponent of the form $Re \sim R_\rho^{-1/4} Ra_\xi^{1/2}$. This latter scaling differs from the one obtained by Hage & Tilgner ([2010](#)) – $Re \sim Ra_\xi |Ra_T|^{-1/2}$ – using experimental data with $Pr \approx 9$ and $Le \approx 230$. Differences between the two could possibly result from the amount of data retained to derive the scalings. Both studies indeed also consider configurations with $R_\rho < 1$ where overturning convection can also develop and modify the scaling behaviours. The development of boundary layers makes the comparison between bounded and unbounded configurations quite delicate, as it requires defining effective quantities measured on the fluid bulk in the bounded configuration (see Radko & Stern [2000](#); Yang *et al.* [2020](#)).

T. Tassin, T. Gastine and A. Fournier

In planetary interiors, fingering convection operates in a quasi-spherical fluid gap enclosed between two rigid boundaries in the case of terrestrial bodies. For terrestrial planets possessing a metallic iron core, the Prandtl number Pr is $O(10^{-1})$, while the Lewis number Le is $O(10^3)$ (e.g. Roberts & King 2013). The depth of the fingering convection region is more uncertain. In any event, it would correspond to a thin shell in the case of Earth, with a ratio between the inner radius r_i and the outer radius r_o larger than $r_i/r_o = 0.9$ (e.g. Labrosse 2015, and references therein), while a deeper shell configuration is more likely for Mercury, since the corresponding fluid layer may be as thick as 880 km (Wardinski *et al.* 2021), yielding a radius ratio close to 0.6. One of the main goals of this study is to assess the applicability of the results derived in local planar geometry to global spherical shells. Because of curvature and the radial changes of the buoyancy force, spherical-shell convection differs from the plane layer configuration and yields asymmetrical boundary layers between both boundaries (e.g. Gastine, Wicht & Aurnou 2015). Only a handful of studies have considered fingering convection in spherical geometry and they all incorporate the effects of global rotation, which makes the comparison with planar models difficult. Silva, Mather & Simitev (2019) and Monville *et al.* (2019) computed the onset of rotating double-diffusive convection in both the fingering and semi-convection regimes. Monville *et al.* (2019) and Guervilly (2022) also considered nonlinear models with $Pr = 0.3$ and $Le = 10$ and observed the formation of large-scale jets. Guervilly (2022) also analysed the scaling behaviour of the horizontal size of the fingers and their mean velocity. At a given rotation speed, the finger size $\mathcal{L}_h$ gradually transits from a large horizontal scale close to onset to decreasing length scales on increasing supercriticality. When rotation becomes less influential, $\mathcal{L}_h$ tends to conform with Stern's scaling. The mean fingering velocity was found to loosely follow the scalings by Brown *et al.* (2013) (see Guervilly's figure 10*b*), deviations from the theory likely occurring because of the imprint of rotation on the dynamics.

While our long-term objective is to conduct global simulations of fingering convection in the presence of global rotation, we opt for an incremental approach. Our immediate goal with the present work is twofold: (i) to assess the salient differences (if any) between fingering convection in global, non-rotating spherical domains and fingering convection in local, non-rotating Cartesian domains; (ii) to examine the occurrence of jet formation in spherical-shell fingering convection. To do so, we conduct a systematic parameter survey of 123 direct numerical simulations in a spherical geometry, varying the Prandtl number between 0.03 and 7, the Lewis number between 3 and 33.3 and the vigour of the forcing up to $Ra_\xi = 5 \times 10^{11}$. The radius ratio of the spherical shell is the same for all simulations. While its value of 0.35 is admittedly smaller than current estimates relevant to planetary interiors (see above), it is meant to exacerbate the differences that may exist between Cartesian and spherical set-ups; such a deep shell is also less demanding on the angular resolution required to resolve fingers, and makes a systematic analysis possible.

The paper is organised as follows: in § 2, we present the governing equations and the numerical model; in § 3 we focus on deriving scaling laws for fingering convection in spherical shells; in § 4, we analyse the formation of jets before concluding in § 5.

2. Model and methods

2.1. *Hydrodynamical model*

We consider a non-rotating spherical shell of inner radius r_i and outer radius r_o with $r_i/r_o = 0.35$ filled with a Newtonian Boussinesq fluid of background density ρ_c. The spherical-shell boundaries are assumed to be impermeable, no slip and held at constant

temperature and chemical composition. The kinematic viscosity ν, the thermal diffusivity κ_T and the diffusivity of chemical composition κ_ξ are assumed to be constant. We adopt the following linear equation of state:

$$\rho = \rho_c[1 - \alpha_T(T - T_c) - \alpha_\xi(\xi - \xi_c)], \tag{2.1}$$

which ascribes changes in density (ρ) to fluctuations of temperature (T) and chemical composition (ξ). In the above expression, T_c and ξ_c denote the reference temperature and composition, while α_T and α_ξ are the corresponding constant expansion coefficients. In the following, we adopt a dimensionless formulation using the spherical-shell gap $d = r_o - r_i$ as the reference length scale and the viscous diffusion time d^2/ν as the reference time scale. Temperature and composition are respectively expressed in units of $\Delta T = T_{top} - T_{bot}$ and $\Delta \xi = \xi_{bot} - \xi_{top}$, their imposed contrasts over the shell. The dimensionless equations which govern the time evolution of the velocity $\boldsymbol{u}$, the pressure p, the temperature T and the composition ξ are expressed by

$$\nabla \cdot \boldsymbol{u} = 0, \tag{2.2}$$

$$\frac{\partial \boldsymbol{u}}{\partial t} + \boldsymbol{u} \cdot \nabla \boldsymbol{u} = -\nabla p + \frac{1}{Pr}\left(-Ra_T T + \frac{Ra_\xi}{Le}\xi\right)ge_r + \nabla^2 \boldsymbol{u}, \tag{2.3}$$

$$\frac{\partial T}{\partial t} + \boldsymbol{u} \cdot \nabla T = \frac{1}{Pr}\nabla^2 T, \tag{2.4}$$

$$\frac{\partial \xi}{\partial t} + \boldsymbol{u} \cdot \nabla \xi = \frac{1}{LePr}\nabla^2 \xi, \tag{2.5}$$

where $\boldsymbol{e}_r$ is the unit vector in the radial direction and $g = r/r_o$ is the dimensionless gravity. The set of equations (2.2)–(2.5) is governed by four dimensionless numbers

$$Ra_T = -\frac{\alpha_T g_o d^3 \Delta T}{\nu \kappa_T}, \quad Ra_\xi = \frac{\alpha_\xi g_o d^3 \Delta \xi}{\nu \kappa_\xi}, \quad Pr = \frac{\nu}{\kappa_T}, \quad Le = \frac{\kappa_T}{\kappa_\xi}, \tag{2.6a–d}$$

termed the thermal Rayleigh, chemical Rayleigh, Prandtl and Lewis numbers, respectively. Our definition of Ra_T makes it negative, in order to stress the stabilising effect of the thermal background. For the sake of clarity, we will also make use of the Schmidt number $Sc = \nu/\kappa_\xi = Le\,Pr$ in the following. The stability of the convective system depends on the value of the density ratio R_ρ (Stern 1960) defined by

$$R_\rho = \frac{\alpha_T \Delta T}{\alpha_\xi \Delta \xi}, \tag{2.7}$$

which relates to the above control parameters via $R_\rho = Le|Ra_T|/Ra_\xi$. In order to compare models with different Lewis numbers Le, it is convenient to also introduce a normalised density ratio r_ρ following Traxler, Garaud & Stellmach (2011a)

$$r_\rho = \frac{R_\rho - 1}{Le - 1}. \tag{2.8}$$

This maps the instability domain for fingering convection, $1 \leq R_\rho < Le$, to $0 \leq r_\rho < 1$.

2.2. *Numerical technique*

We consider numerical simulations computed using the pseudo-spectral open-source code MagIC (freely available at https://github.com/magic-sph/magic) (Wicht 2002). MagIC has

been validated against a benchmark for rotating double-diffusive convection in spherical shells initiated by Breuer *et al.* (2010). The system of equations (2.2)–(2.5) is solved in spherical coordinates (r, θ, ϕ), expressing the solenoidal velocity field in terms of poloidal (W) and toroidal (Z) potentials

$$\boldsymbol{u} = \boldsymbol{u}_P + \boldsymbol{u}_T = \nabla \times (\nabla \times W \boldsymbol{e}_r) + \nabla \times Z \boldsymbol{e}_r. \tag{2.9}$$

The unknowns W, Z, p, T and ξ are then expanded in spherical harmonics up to the maximum degree ℓ_{max} and order $m_{max} = \ell_{max}$ in the angular directions. Discretisation in the radial direction involves a Chebyshev collocation technique with N_r collocation grid points (Boyd 2001). The equations are advanced in time using the third-order implicit–explicit Runge–Kutta schemes ARS343 (Ascher, Ruuth & Spiteri 1997) and BPR353 (Boscarino, Pareschi & Russo 2013) which handle the linear terms of (2.2)–(2.5) implicitly. At each iteration, the nonlinear terms are calculated on the physical grid space and transformed back to spectral representation using the open-source SHTns library (freely available at https://gricad-gitlab.univ-grenoble-alpes.fr/schaeffn/shtns) (Schaeffer 2013). The seminal work by Glatzmaier (1984) and the more recent review by Christensen & Wicht (2015) provide additional insights into the algorithm (the interested reader may also consult Lago *et al.* (2021) with regard to its parallel implementation).

2.3. *Diagnostics*

We introduce here several diagnostics that will be used to characterise the convective flow and the thermal and chemical transports. We hence adopt the following notations to denote temporal and spatial averaging of a field f:

$$\bar{f} = \frac{1}{t_{avg}} \int_{t_0}^{t_0+t_{avg}} f \, \mathrm{d}t, \quad \langle f \rangle_V = \frac{1}{V} \int_V f \, \mathrm{d}V, \quad \langle f \rangle_S = \frac{1}{4\pi} \int_0^{2\pi} \int_0^{\pi} f \sin\theta \, \mathrm{d}\theta \, \mathrm{d}\phi, \tag{2.10a–c}$$

where time averaging runs over the interval $[t_0, t_0 + t_{avg}]$, V is the spherical shell volume and S is the unit sphere. Time-averaged poloidal and toroidal energies are defined by

$$E_{k,pol} = \frac{1}{2}\overline{\langle \boldsymbol{u}_P \cdot \boldsymbol{u}_P \rangle_V} = \sum_{\ell=1}^{\ell_{max}} E_{k,pol}^{\ell}, \quad E_{k,tor} = \frac{1}{2}\overline{\langle \boldsymbol{u}_T \cdot \boldsymbol{u}_T \rangle_V} = \sum_{\ell=1}^{\ell_{max}} E_{k,tor}^{\ell}, \tag{2.11a,b}$$

noting that both can be expressed as the sum of contributions from each spherical harmonic degree ℓ, $E_{k,pol}^{\ell}$ and $E_{k,tor}^{\ell}$. The corresponding Reynolds numbers are then expressed by

$$Re_{pol} = \sqrt{2E_{k,pol}}, \quad Re_{tor} = \sqrt{2E_{k,tor}}. \tag{2.12a,b}$$

In the following we also employ the chemical Péclet number, Pe, to quantify the vertical velocity. It relates to the Reynolds number of the poloidal flow via

$$Pe = Re_{pol} \, Sc. \tag{2.13}$$

We introduce the notation Θ and Ξ to define the time and horizontally averaged radial profiles of temperature and chemical composition

$$\Theta = \overline{\langle T \rangle_S}, \quad \Xi = \overline{\langle \xi \rangle_S}. \tag{2.14a,b}$$

Heat and chemical composition transports are defined at all radii by the Nusselt Nu and Sherwood Sh numbers

$$Nu = \frac{\overline{\langle u_r T \rangle_S} - \dfrac{1}{Pr}\dfrac{d\Theta}{dr}}{-\dfrac{1}{Pr}\dfrac{dT_c}{dr}}, \quad Sh = \frac{\overline{\langle u_r \xi \rangle_S} - \dfrac{1}{Sc}\dfrac{d\Xi}{dr}}{-\dfrac{1}{Sc}\dfrac{d\xi_c}{dr}}, \quad (2.15a,b)$$

where $dT_c/dr = r_i r_o/r^2$ and $d\xi_c/dr = -r_i r_o/r^2$ are the gradients of the diffusive states. In the numerical computations, those quantities are practically evaluated at the outer boundary, $r = r_o$, where the convective fluxes vanish. Heat sinks and sources in fingering convection are provided by buoyancy power of thermal and chemical origins $\mathcal{P}_T$ and $\mathcal{P}_\xi$, expressed by

$$\mathcal{P}_T = \frac{|Ra_T|}{Pr}\overline{\langle g u_r T \rangle_V}, \quad \mathcal{P}_\xi = \frac{Ra_\xi}{Sc}\overline{\langle g u_r \xi \rangle_V}. \quad (2.16a,b)$$

On time average, the sum of these two buoyancy sources balances the viscous dissipation D_ν according to

$$\mathcal{P}_T + \mathcal{P}_\xi = D_\nu, \quad (2.17)$$

where $D_\nu = \overline{\langle (\nabla \times \boldsymbol{u})^2 \rangle_V}$.

As shown in Appendix B, the thermal and compositional buoyancy powers can be approximated in spherical geometry by

$$\mathcal{P}_T \approx -\frac{4\pi r_i r_m}{V}\frac{|Ra_T|}{Pr^2}(Nu - 1), \quad \mathcal{P}_\xi \approx \frac{4\pi r_i r_m}{V}\frac{Ra_\xi}{Sc^2}(Sh - 1), \quad (2.18a,b)$$

where $r_m = (r_o + r_i)/2$ is the mid-shell radius. The turbulent flux ratio (Traxler *et al.* 2011*a*) is defined by

$$\gamma = R_\rho \frac{|\langle u_r T \rangle_V|}{\langle u_r \xi \rangle_V} \approx R_\rho Le \frac{Nu - 1}{Sh - 1}. \quad (2.19)$$

The typical flow length scale is estimated using an integral length scale (see Backus, Parker & Constable 1996, § 3.6.3)

$$\mathcal{L}_h = \frac{\pi r_m}{\sqrt{\ell_h(\ell_h + 1)}} \approx \frac{\pi r_m}{\ell_h}, \quad (2.20)$$

in which the average spherical harmonic degree ℓ_h is defined according to

$$\ell_h = \frac{\sum_{\ell,m} \ell \mathcal{E}_\ell^m}{\sum_{\ell,m} \mathcal{E}_\ell^m}, \quad (2.21)$$

where $\mathcal{E}_\ell^m$ denotes the time and radially averaged poloidal kinetic energy at degree ℓ and order m. Note that this global ℓ_h is what uniquely defines the flow length scale, and is routinely used as a diagnostic in global spherical simulations (e.g. Christensen & Aubert 2006). One could define a radially varying ℓ_h, by considering the radial profiles of the spherical harmonic expansion of the kinetic poloidal energy, and obtain accordingly $\mathcal{L}_h(r)$. Preliminary inspections revealed no sizeable changes of $\mathcal{L}_h(r)$ in the fluid bulk, and led us to stick to the integral definition given above for the sake of parsimony.

Name	Notation	Definition	This study
Thermal Rayleigh	$|Ra_T|$	$|\alpha_T g_o \mathcal{D}^3 \Delta T / \nu \kappa_T|$	$7.334 \times 10^4 - 1.83 \times 10^{11}$
Chemical Rayleigh	Ra_ξ	$\alpha_\xi g_o \mathcal{D}^3 \Delta \xi / \nu \kappa_\xi$	$2 \times 10^5 - 5 \times 10^{11}$
Prandtl	Pr	ν / κ_T	$0.03 - 7$
Schmidt	Sc	ν / κ_ξ	$1 - 30$
Lewis	Le	κ_T / κ_ξ	$3 - 33.3$
Density ratio	R_ρ	$Le|Ra_T| / Ra_\xi$	$1 - Le$

Table 1. Name, notation, definition and range covered by the dimensionless control parameters employed in this study.
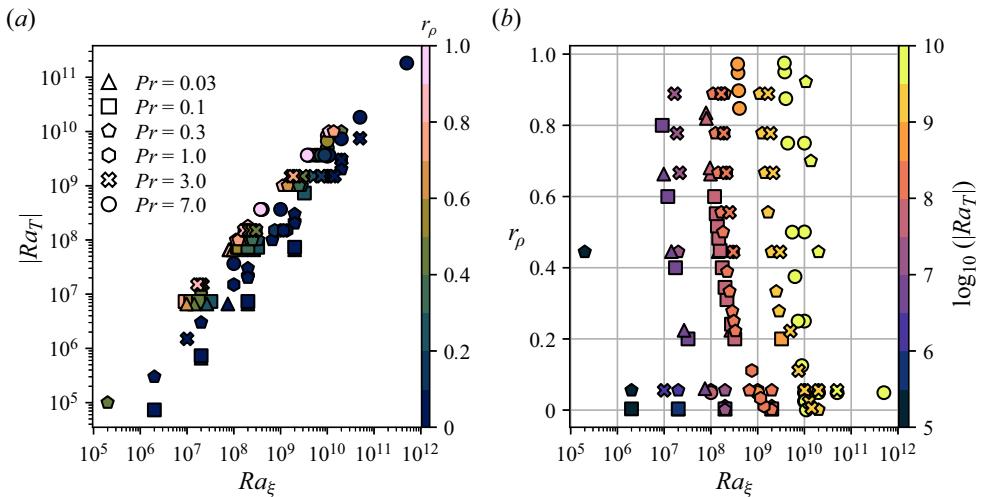

Figure 1. (*a*) Normalised density ratio r_ρ in the thermal Rayleigh number $|Ra_T|$–chemical Rayleigh number Ra_ξ plane for the 123 simulations performed for this study; (*b*) $\log_{10}(|Ra_T|)$ in the Ra_ξ–r_ρ plane for the same simulations. Markers reflect the value of Pr.

2.4. *Parameter coverage*

Table 1 summarises the parameter space covered by this study. In order to compare our results against previous numerical studies by e.g. Stellmach *et al.* (2011), Traxler *et al.* (2011*a*), Brown *et al.* (2013) and Yang *et al.* (2016), the Prandtl number Pr spans two orders of magnitude, from 0.03 to 7, while the Lewis number Le varies from 3 to 33.3. The thermal and chemical Rayleigh numbers Ra_T and Ra_ξ are between -1.83×10^{11} and -7.33×10^4, and 2×10^5 and 5×10^{11}, respectively, thereby permitting an extensive description of the primary instability region for each value of the Lewis number Le (recall (1.1)). In practice, this coverage leads to a grand total of 123 simulations.

Figure 1 illustrates the exploration of the parameter space. Subsets of simulations were designed according to three different strategies. First, by varying (Ra_T, Ra_ξ), hence the buoyancy input power, while keeping the triplet (Pr, Le, R_ρ) constant. This gives rise to the horizontal lines in figure 1(*b*). Second, by varying Ra_ξ, and consequently R_ρ, at constant (Pr, Le, Ra_T). These series are located on the horizontal lines in figure 1(*a*), and along branches of the same colour in figure 1(*b*), see e.g. the yellow circles with $Ra_\xi \lesssim 10^{10}$. This subset is meant to ease the comparison with previous local studies in periodic Cartesian

boxes, where the box size is set according to the number of fingers it contains, which amounts to an implicit prescription of Ra_T. Third, we performed a series by varying Ra_T, keeping (Pr, Le, Ra_ξ) constant. It shows as a vertical line of 5 circles in both panels of figure 1, noting that Ra_ξ is set to 10^{10} for this series.

On the technical side, the spatial resolution ranges from $(N_r, \ell_{max}) = (41, 85)$ to $(769, 938)$ in the catalogue of simulations, notwithstanding a single simulation that used finite differences in radius with 1536 grid points in conjunction with $\ell_{max} = m_{max} = 1536$. Moderately supercritical cases were initialised by a random thermo-chemical perturbation applied to a motionless fluid. The integration of strongly supercritical cases started from snapshots of equilibrated solutions subject to weaker forcings, in order to shorten the duration of the transient regime. Numerical convergence was in most cases assessed by checking that the average power balance defined by (2.17) was satisfied within 2 % (King, Stellmach & Aurnou 2012). In some instances, however, the emergence and growth of jets caused the solution to evolve over several viscous time scales τ_ν without reaching a statistically converged state in the power balance sense. The convergence criterion we used instead was that of a stable cumulative temporal average of $E_{k,tor}$, which we assessed by visual inspection. For five strongly driven simulations, jets did not reach their saturated state because of a too costly numerical integration; this may result in an underestimated value of $E_{k,tor}$. These five cases feature a 'NS' label in the leftmost column of table 3, where the main properties of the 123 simulations are listed. The total computation time required for this study represents 20 million single core hours, executed for the most part on AMD Rome processors.

2.5. *Definition of boundary layers*

We now turn our attention to the practical characterisation of the boundary layers that emerge in our bounded set-up, whose properties are governed by the least diffusive field, i.e. the chemical composition (e.g. Radko & Stern 2000). In the remainder of this study, λ_i (respectively λ_o) will denote the thickness of the inner (respectively outer) chemical boundary layer. In contrast to planar configurations, boundary layer thicknesses at both boundaries differ ($\lambda_i \neq \lambda_o$) due to curvature and radial changes of the gravitational acceleration (e.g. Vangelov & Jarvis 1994; Gastine *et al.* 2015). Figure 2(*a*) shows the time-averaged radial profiles of convective and diffusive chemical fluxes (recall (2.15*a,b*)), alongside the variance of chemical composition, $\sigma_\xi(r)$, for a simulation with $|Ra_T| = 3.66 \times 10^7$, $R_\rho = 1.1$, $Pr = 7$ and $Le = 3$ (simulation 123 in table 3). Several methods have been introduced to assess the boundary layer thicknesses. An account of these approaches is given by Julien *et al.* (2012, § 2.2), in the classical context of Rayleigh–Bénard convection in planar geometry. In that set-up, temperature is uniform within the convecting bulk, and a first approach consists of picking the depth at which the linear profile within the thermal boundary layer intersects the temperature of the convecting core (see also Belmonte, Tilgner & Libchaber 1994, their figure 3). A second possibility is to argue that the depth of the boundary layer is that at which the standard deviation of temperature reaches a local maximum (e.g. Tilgner, Belmonte & Libchaber 1993, their figure 4). Long *et al.* (2020) showed, however, that both approaches become questionable when convection operates under the influence of global rotation, in which case the heterogeneous distribution of temperature causes the linear intersection method to fail, or if Neumann boundary conditions are prescribed in place of Dirichlet conditions for the temperature field, then the maximum variance method is no longer adequate. A third option proposed by Julien *et al.* (2012), and favoured by Long *et al.* (2020) in

their study, is to define λ_i and λ_o at the locations where convective and diffusive fluxes are equal. Chemical boundary layers defined by this condition appear as blue-shaded regions in figure 2. They are thinner than those that may have been determined otherwise using either the linear intersection or the standard deviation approaches (Julien *et al.* 2012) and they are asymmetric, with $\lambda_i < \lambda_o$. Figure 2(*b*) shows the time-averaged radial profiles of temperature and composition. We observe a pronounced asymmetry in both profiles with a larger temperature and composition drop accommodated across the inner boundary layer than across the outer one. Inspection of figure 2(*b*) also reveals that the profiles of composition and temperature remain quite close to linear within the boundary layers determined with the flux equipartition method. In the following, we will adhere to this approach, and exploit the linearity of the profiles of temperature and composition in some of our derivations. The downside of this choice is that it does not incorporate the curvy part of the profiles at the edge of the boundary layers, hence possibly overestimating the contrast of composition in the fluid bulk compared with other boundary layer definitions.

Let λ_b denote the thickness of the bulk of the fluid permeated by fingers, let $\Delta_b\Theta$ and $\Delta_b\varXi$ stand for the contrast of temperature and composition across this region and let $\Delta_i\varXi$ ($\Delta_o\varXi$) and $\Delta_i\Theta$ ($\Delta_o\Theta$) be the composition and temperature drops across the inner (outer) chemical boundary layer. By choice, each contrast is a positive quantity. We note for future usage that the following non-dimensional relationships hold:

$$1 = \lambda_i + \lambda_b + \lambda_o, \quad 1 = \Delta_i\Theta + \Delta_b\Theta + \Delta_o\Theta, \quad 1 = \Delta_i\varXi + \Delta_b\varXi + \Delta_o\varXi.$$
$$(2.22a\text{–}c)$$

3. Fingering convection

3.1. *Flow morphology*

We first focus on a series of three simulations to highlight the specificities of fingering convection in global spherical geometry. Figure 3 provides three-dimensional renderings of the fingers, along with the corresponding kinetic energy spectra, of three cases that share $R_\rho = 1.1$, $Pr = 7$ and $Le = 3$ and differ by Ra_ξ, which increases from 10^8 to 2×10^{10} (simulations 123, 118 and 103 in table 3). The convective power injected in the fluid is accordingly multiplied by 500 between the simulation closest to onset, illustrated in figure 3(*a*), and the most supercritical one, shown in figure 3(*c*). For the least forced simulation (figure 3*a*), the flow is dominated by coherent radial filaments that extend over the entire spherical shell. These particular structures are reminiscent of the 'elevator modes' found in periodic planar models (e.g. Radko 2013, § 2.1). Inside each of these filaments T, ξ and u_r can be considered to be quasi-uniform. The velocity field reaches relatively small amplitudes, with a poloidal Reynolds number $Re_{pol} \approx 10$. Geometrical patterns link the fingers together over spherical surfaces, and it appears that fingers emerge at the vertices of polygons in the vicinity of the inner sphere. Fingers have an almost constant width in the bulk of the domain. The rather large polygonal patterns that appear on the outer surface of the three-dimensional rendering are due to the weakening of the radial velocity in the vicinity of the outer boundary layer, that goes along with a widening of the finger as it penetrates the boundary layer. The spectrum of this simulation, displayed in figure 3(*d*), presents a marked maximum, with an average spherical harmonic degree ℓ_h (recall (2.21)) of 39. The majority of the poloidal kinetic energy of the fluid is stored in degrees close to this peak. The quasi-homogeneous lateral thickness of fingers in figure 3(*a*) illustrates this spectral concentration.

Figure 3(*b*) reveals that a strengthening of the forcing leads to an increase of the magnitude of the velocity, with $Re_{pol} = 28$, alongside a gradual loss of the coherent tubular

988 A18-10
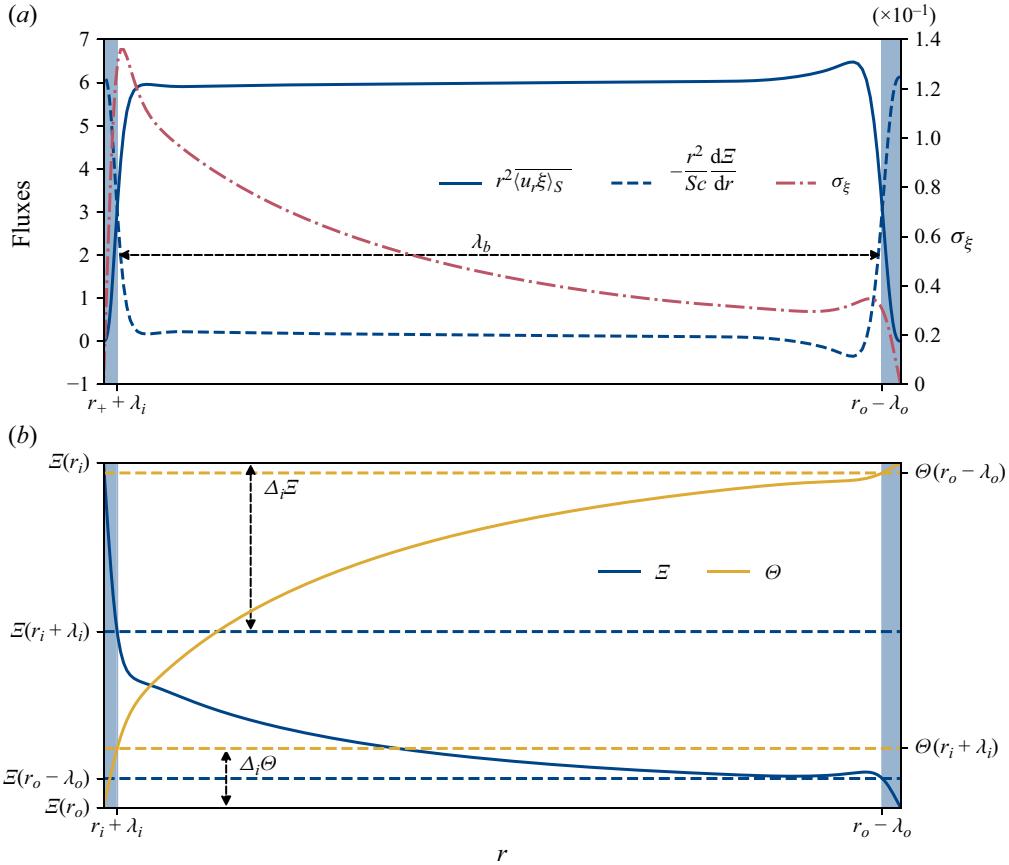
Figure 2. (*a*) Time-averaged radial profiles of convective and diffusive compositional fluxes, expressed by $r^2\overline{\langle u_r\xi\rangle_S}$ and $-r^2 Sc^{-1}\,\mathrm{d}\Xi/\mathrm{d}r$ respectively (see (2.15*a*,*b*)), for a simulation with $|Ra_T| = 3.66 \times 10^7$, $R_\rho = 1.1$, $Pr = 7$ and $Le = 3$ (simulation 123 in table 3). The radial profile of the variance of composition σ_ξ is represented by a dash-dotted line. (*b*) Time-averaged radial profiles of composition (solid blue line) and temperature (solid mustard line). Horizontal dashed lines highlight the values of composition and temperature at the edges of the convective bulk. Here, $\Delta_i\Xi$ ($\Delta_i\Theta$) is the composition (temperature) drop across the inner boundary layer. The blue-shaded areas highlight the inner and outer chemical boundary layers, of thickness λ_i and λ_o, respectively, while the convective bulk has a thickness λ_b.

structure of the fingers in favour of undulations and occasional branchings. They contract horizontally, leading to a shift of ℓ_h to a higher value of 75. The geometrical patterns remain well defined over the inner sphere but appear attenuated at the outer spherical surface, again the signature of the effect of the outer boundary layer. Further increase of the injected convective power causes the occasional fracture of fingers in the radial direction, see figure 3(*c*), as they assume the shape of flagella reminiscent of the modes of Holyer (1984, figure 1). Although the fingers gradually lose their vertical coherence with increased convective forcings, they still present an anisotropic elongated structure in the radial direction. Accordingly, the lateral thickness of the fingers continues to decrease and ℓ_h now reaches a value of 166. That amounts to finding $O(10^4)$ such elongated structures at any radius r in the bulk of the flow.
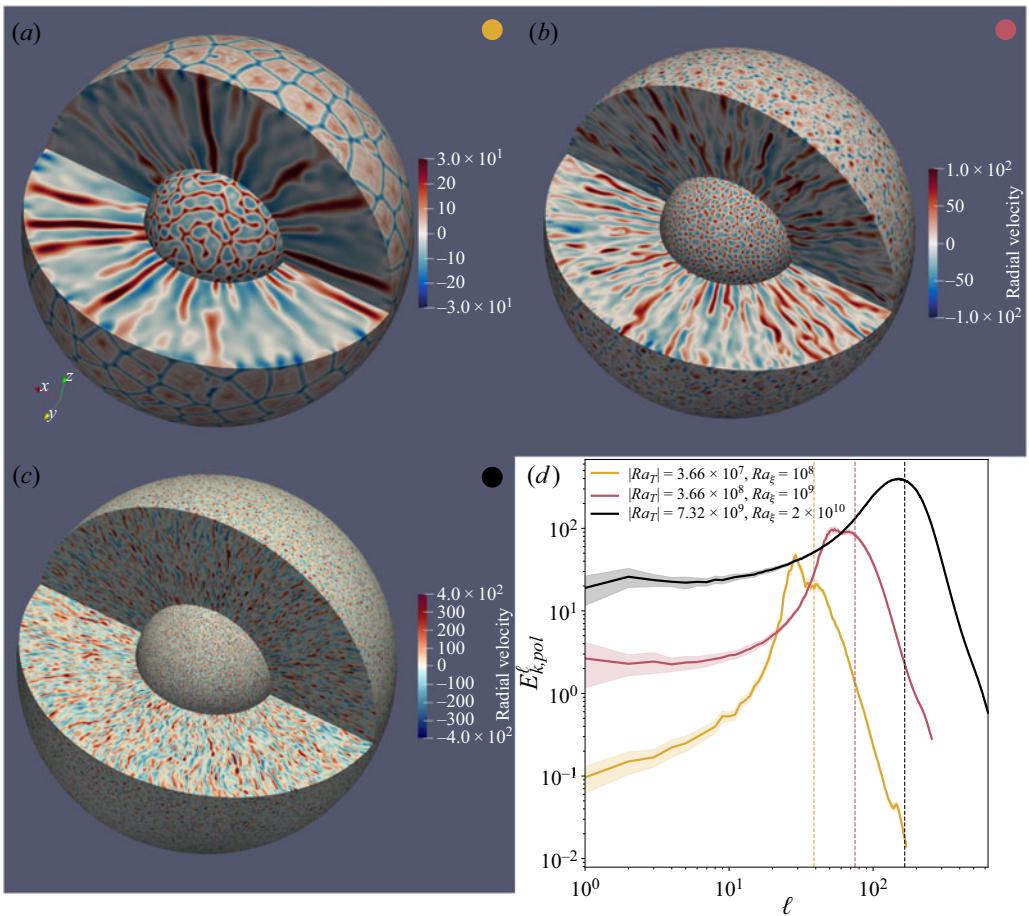
Figure 3. (*a*–*c*) Three-dimensional renderings of the radial velocity for three simulations carried out using $R_\rho = 1.1$, $Pr = 7$ and $Le = 3$, and $Ra_\xi = 10^8$, 10^9 and 2×10^{10} (simulations 123, 118 and 103 in table 3), for (*a*), (*b*) and (*c*), respectively. Inner and outer spherical surfaces correspond to $r_i + 0.03$ and $r_o - 0.04$, respectively. (*d*) Poloidal kinetic energy spectra as a function of spherical harmonic degree ℓ for these three simulations. Dashed vertical lines correspond to the average spherical harmonic degree ℓ_h (see (2.21)), of value 39, 75 and 166, for $Ra_\xi = 10^8$, 10^9 and 2×10^{10}.

3.2. *Mean profiles and compositional boundary layers*

We now assess the impact of fingers on the average temperature and composition profiles within the spherical shell. Figure 4(*a*,*b*) shows the time-averaged radial profiles of temperature and composition of four simulations that share $|Ra_T| = 3.66 \times 10^9$, $Pr = 7$, $Le = 3$ and differ by the prescribed Ra_ξ, whose value goes from 4.392×10^9 to 1.1×10^{10}, with a concomitant decrease of r_ρ from 0.75 down to 5×10^{-4}.

The increase of Ra_ξ impacts composition more than temperature, as it leads to steeper boundary layers and flatter bulk profiles of ξ that substantially deviate from their diffusive reference, displayed with a dashed line in figure 4(*b*). Inspection of figure 4(*a*) shows that this trend exists but is less marked for temperature. Accordingly, the bulk temperature and composition drops, $\Delta_b\Theta$ and $\Delta_b\Xi$, introduced above decrease as Ra_ξ increases, in a much more noticeable manner for composition than for temperature. Boundary layer asymmetry inherent in curvilinear geometries (Jarvis 1993) is clearer with increasing Ra_ξ: for the

988 A18-12
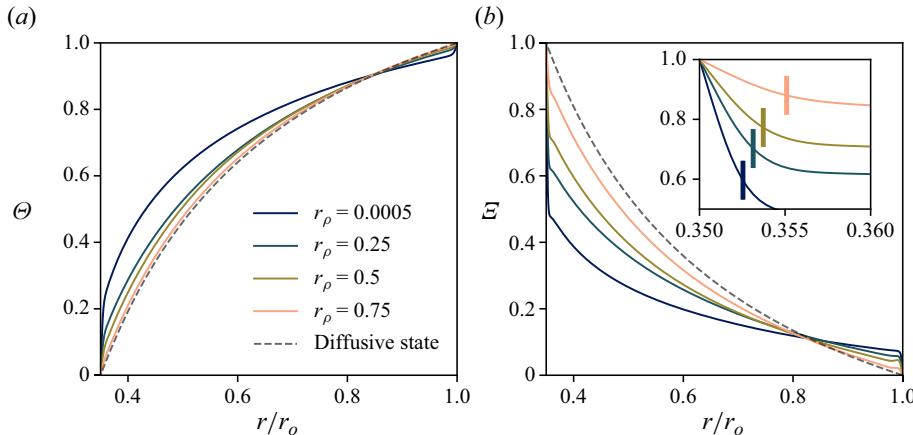
Figure 4. (*a*) Time-averaged radial profile of temperature, Θ, for four simulations sharing $|Ra_T| = 3.66 \times 10^9$, $Pr = 7$ and $Le = 3$, and increasing values of r_ρ (simulations 106, 110, 112 and 113 in table 3). (*b*) Time-averaged radial profile of composition, Ξ, for the same simulations. The inset shows a magnification of the inner boundary layer, whose edge is shown with a thick vertical segment. In both panels, the dashed lines correspond to the diffusive reference profile.

largest forcing considered here, approximately 40 % (10 %) of the contrast of composition is accommodated at the inner (outer) boundary layer.

To enable comparison with results from unbounded studies, we seek scaling laws for the effective contrasts $\Delta_b \Theta$ and $\Delta_b \Xi$ that develop in the fluid bulk. To that end, and in line with the characterisation of boundary layers we introduced above, we first make use of the heat and composition flux conservation over spherical surfaces. Assuming that temperature and composition vary linearly within boundary layers yields

$$\left(\frac{r_i}{r_o}\right)^2 \frac{\Delta_i \Theta}{\Delta_o \Theta} = \frac{\lambda_i}{\lambda_o}, \quad \left(\frac{r_i}{r_o}\right)^2 \frac{\Delta_i \Xi}{\Delta_o \Xi} = \frac{\lambda_i}{\lambda_o}, \tag{3.1a,b}$$

where the r_i/r_o factors emphasise the asymmetry of the boundary layer properties caused by the spherical geometry. To derive scaling laws for the ratio of the temperature and composition drops at both boundary layers, one must invoke a second hypothesis. In classical Rayleigh–Bénard convection in an annulus, Jarvis (1993) made the additional assumption that the boundary layers are marginally unstable (Malkus 1954). In other words, a local Rayleigh number defined on the boundary layer thickness should be close to the critical value to trigger convection. Later numerical simulations in three dimensions by Deschamps, Tackley & Nakagawa (2010) in the context of infinite Prandtl number convection and by Gastine *et al.* (2015) for $Pr = 1$, however, showed that this hypothesis failed to correctly account for the actual boundary layer asymmetry observed in spherical geometry. For fingering convection in bounded domains, Radko & Stern (2000) nonetheless showed that the marginal stability argument provides a reasonable description of the boundary layers for composition. We here test this hypothesis by introducing the local thermohaline Rayleigh numbers Ra^{λ_i} and Ra^{λ_o} defined over the extent of the inner and outer boundary layers

$$Ra^{\lambda_i} = g_i \lambda_i^3 \left(Ra_\xi \Delta_i \Xi - |Ra_T| \Delta_i \Theta\right), \quad Ra^{\lambda_o} = g_o \lambda_o^3 \left(Ra_\xi \Delta_o \Xi - |Ra_T| \Delta_o \Theta\right), \tag{3.2a,b}$$

where g_i and g_o denote the acceleration due to gravity at the inner and outer boundaries, with $g_i/g_o = r_i/r_o$. We note in passing that gravity increasing linearly with radius is the second factor responsible for the boundary layer asymmetry. Equating Ra^{λ_i} and Ra^{λ_o} to a critical value Ra^c gives, in light of (3.1*a*,*b*),

$$\left(\frac{\lambda_i}{\lambda_o}\right)^3 = \frac{r_o}{r_i}\frac{\Delta_o \Xi}{\Delta_i \Xi}. \tag{3.3}$$

Further use of (3.1*a*,*b*) yields

$$\frac{\lambda_o}{\lambda_i} = \left(\frac{r_i}{r_o}\right)^{-1/4}, \tag{3.4}$$

and

$$\frac{\Delta_o \Xi}{\Delta_i \Xi} = \left(\frac{r_i}{r_o}\right)^{7/4}, \tag{3.5}$$

both of which are a function of the sole radius ratio r_i/r_o.

Figure 5 shows the conformity of these two laws to the numerical dataset, which has a constant radius ratio $r_i/r_o = 0.35$. In figure 5(*a*), we observe a close to linear increase of λ_o with λ_i over two orders of magnitude of variations. A least-squares fit performed for those simulations with $\lambda_i < 0.02$ provides $\lambda_o = 1.18\,\lambda_i$ instead of the expected $\lambda_o = 1.30\,\lambda_i$ from (3.4). Simulations causing this departure are those close to onset with thick boundary layers within which the linearity assumption may not hold. Likewise, we see in figure 5(*b*) that (3.5) captures the relative ratio $\Delta_o \Xi / \Delta_i \Xi$ within the dataset. We find $\Delta_o \Xi = 0.14 \Delta_i \Xi$ instead of the predicted $\Delta_o \Xi = 0.16 \Delta_i \Xi$, and note that the dispersion about a linear law is maximum for strongly driven simulations (those with smaller r_ρ in figure 5*b*). These results indicate that, in contrast with Rayleigh–Bénard convection, the marginal stability hypothesis provides a good way to characterise the boundary layer asymmetry in spherical-shell fingering convection, with the caveat that confirmation of this finding should be sought for radius ratios other than the one considered in this study.

In order to obtain a relationship between the contrasts across the bulk, $\Delta_b \Xi$ and $\Delta_b \Theta$, recall that the Sherwood and Nusselt numbers *Sh* and *Nu* are expected to read at $r = r_o$

$$Sh = \frac{r_o}{r_i}\frac{\Delta_o \Xi}{\lambda_o}, \quad Nu = \frac{r_o}{r_i}\frac{\Delta_o \Theta}{\lambda_o}, \tag{3.6a,b}$$

if the linearity assumption for composition and temperature holds within the chemical boundary layer. Combining these definitions with (2.22*a*–*c*) and (3.4)–(3.5) yields the following relationship between $\Delta_b \Theta$, $\Delta_b \Xi$, *Nu* and *Sh*:

$$\frac{1 - \Delta_b \Xi}{1 - \Delta_b \Theta} = \frac{Sh}{Nu}. \tag{3.7}$$

Figure 6(*a*) shows that there is convincing evidence for a linear relationship between $(1 - \Delta_b \Xi)/(1 - \Delta_b \Theta)$ and *Sh*/*Nu* across the parameter space sampled by the dataset; the slope is equal to 0.84 instead of the expected value of one. This might come from the uncertainty related to the departure from the linearity assumption for the chemical boundary layer, possibly leading to underestimation of the true value of the Sherwood number.
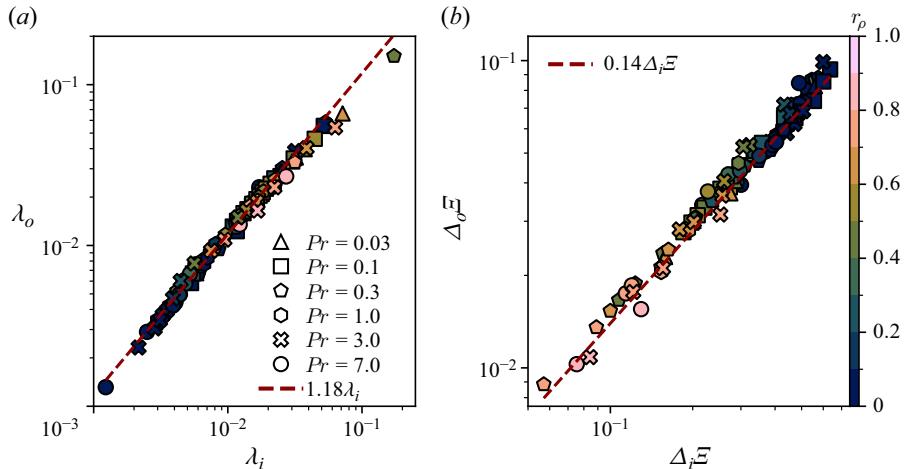
Figure 5. (*a*) Thickness of the outer boundary layer, λ_o, as a function of the thickness of the inner boundary layer, λ_i. (*b*) Composition contrast across the outer boundary layer, $\Delta_o \Xi$, as a function of its inner counterpart, $\Delta_i \Xi$. In both panels, the dashed lines correspond to a linear fit to data retaining only those simulations with $\lambda_i < 0.02$.
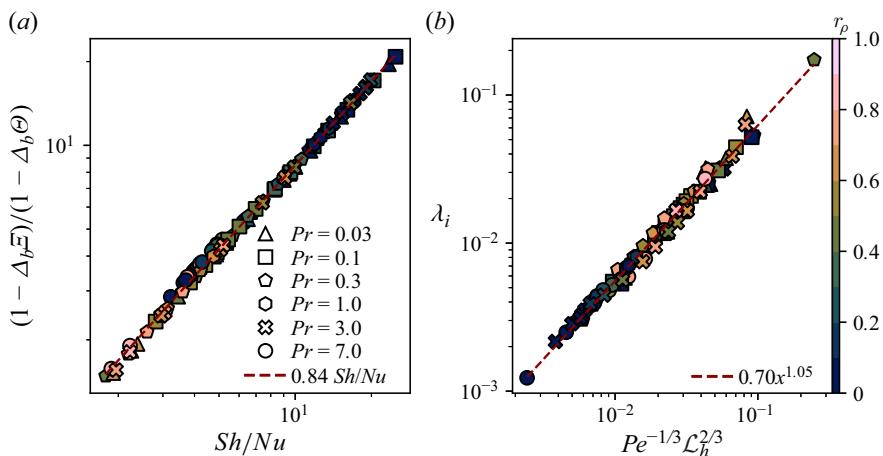
Figure 6. (*a*) Value of $(1 - \Delta_b \Xi)/(1 - \Delta_b \Theta)$ as a function of Sh/Nu. (*b*) Thickness of the inner boundary layer as a function of $Pe^{-1/3}\mathcal{L}_h^{2/3}$ derived in (3.12). In each panel, the result of the linear regression is shown with a dashed line.

For a better understanding of (3.7), it is insightful to split the mean radial profiles into the sum of a reference conducting state and fluctuations denoted by primed quantities

$$\Xi = \xi_c + \Xi', \quad \Theta = T_c + \Theta'. \tag{3.8a,b}$$

Using the definition of the flux ratio (2.19), (3.7) can be rewritten as

$$\frac{\Delta_b \Xi'}{\Delta_b \Theta'} \approx R_\rho Le \gamma^{-1}, \tag{3.9}$$

where we have assumed that $\Delta_b \xi_c = \Delta_b T_c \approx 1$.

Following Yang *et al.* (2015), we now evaluate whether results coming from classical Rayleigh–Bénard convection models regarding the nature of the boundary layers are

still applicable to bounded double-diffusive convection. In that regard, the cornerstone of the GL theory is that the kinetic and thermal boundary layer thicknesses adhere to the Prandtl–Blasius model (e.g. Schlichting & Gersten 2018, § 9.2). In this model, the boundary layer corresponds to a laminar flow over a horizontal plate and the temperature and chemical composition are treated as passive scalars. For fingering convection with $Le > 1$, this translates to

$$\frac{\lambda_\xi}{\mathcal{L}_h} \sim Sc^{-1/2} Re_h^{-1/2} (Sc < 1), \quad \frac{\lambda_\xi}{\mathcal{L}_h} \sim Sc^{-1/3} Re_h^{-1/2} (Sc > 1), \tag{3.10a,b}$$

where λ_ξ denotes the thickness of the inner or outer chemical boundary layer, and $Re_h = u_h \mathcal{L}_h / \nu$ is a Reynolds number defined using the length scale $\mathcal{L}_h$ and the near-boundary horizontal flow velocity u_h. For tubular fingers, mass conservation between the finger core of typical diameter λ_ξ (Yang *et al.* 2016, their figure 10) and the horizontal flows that converge towards the finger in the boundary layers demands

$$u_h \lambda_\xi \pi \mathcal{L}_h \approx u_r \frac{\pi}{4} \lambda_\xi^2 \ (Sc < 1), \quad \frac{\lambda_\xi}{\lambda_U} u_h \lambda \pi \mathcal{L}_h \approx u_r \frac{\pi}{4} \lambda_\xi^2 \ (Sc > 1), \tag{3.11a,b}$$

where λ_U denotes the thickness of the velocity boundary layer. The factor λ_ξ / λ_U in the equation on the right reflects the fact that the velocity boundary layer is nested in the compositional one when $Sc > 1$. As such, and assuming linear boundary layers, the relevant horizontal flow velocity has to be rescaled by the relative thickness of both boundary layers. Using (3.10a,b), this then leads to the unique form

$$\lambda_\xi \sim Pe^{-1/3} \mathcal{L}_h^{2/3}, \tag{3.12}$$

for both Schmidt number end members. Figure 6(b) shows the thickness of the inner compositional boundary layer ($\lambda_\xi = \lambda_i$) as a function of this theoretical scaling for all the simulations where the boundary layers could be evaluated. The reduced scatter of the data as well as the slope of the best fit power law being close to one indicate an excellent agreement with the Prandtl–Blasius model combined with the hypothesis of tubular fingers.

3.3. *Effective density ratio*

In order to compare the dynamics with unbounded domains, the common practice in bounded planar geometry (Schmitt 1979b; Radko & Stern 2000; Yang *et al.* 2020) consists in introducing an effective density ratio within the bulk of the domain expressed by

$$R_\rho^\star = R_\rho \frac{\Delta_b \Theta}{\Delta_b \Xi}. \tag{3.13}$$

This measure is appropriate to fingering convection in Cartesian domains with $R_\rho \ll Le$, given the piecewise-linear nature of the composition profile (see e.g. figure 2 of Yang 2020). This estimate is, however, not suitable close to onset as the boundary layer definition becomes ill posed. An extra complication arises in spherical geometry since our definition of boundary layers only retains the linear part of the drop of composition, which tends to overestimate $\Delta_b \Xi$ (recall figure 2 and the discussion in § 2.5). As such, it appears more reliable to introduce an effective density ratio (and its normalised counterpart) based on

the gradients of temperature and composition at mid-depth

$$R_\rho^\star = -R_\rho \left.\frac{d\Theta}{dr}\right|_{r_m} \left(\left.\frac{d\Xi}{dr}\right|_{r_m}\right)^{-1}, \quad r_\rho^\star = \frac{R_\rho^\star - 1}{Le - 1}. \tag{3.14a,b}$$

We saw above that the contrast of composition across the bulk (or fingering region) is systematically lower than that of temperature. It hence follows that $R_\rho^\star > R_\rho$ and $r_\rho^\star > r_\rho$.

3.4. *Finger width*

We now derive scaling laws for fingering convection based on our 123 bounded simulations, beginning with the typical lateral extent $\mathcal{L}_h$ of a finger, as defined in (2.21). In his seminal contribution, Stern (1960) predicts a scaling of the form

$$\mathcal{L}_h \propto |Ra_T|^{-1/4}, \tag{3.15}$$

for an unbounded Boussinesq fluid subjected to uniform thermal and chemical background gradients when $Le \gg R_\rho \gg 1$. A least-squares fit of our dataset yields

$$\mathcal{L}_h = 4.23 \, |Ra_T|^{-0.23}, \tag{3.16}$$

where the exponent found is rather close to the expected value of -0.25, for values of $|Ra_T|$ spanning 6 orders of magnitude. Yet, inspection of figure 7(*a*) reveals that this scaling fails to capture a second dependency to r_ρ. At a given value of $|Ra_T|$, we observe indeed that $\mathcal{L}_h$ is an increasing function of r_ρ. In order to make progress, let us assume that the finger width is controlled by a balance between buoyancy and viscous forces. In addition, we resort to the tall finger hypothesis introduced by Stern (1975, p. 192) and christened by Smyth & Kimura (2007), which consists of neglecting along-finger derivatives in favour of cross-finger derivatives. Accordingly, the time and volume average of the radial component of (2.3) becomes

$$\overline{\left\langle \left(-\frac{Ra_T}{Pr}T + \frac{Ra_\xi}{LePr}\xi\right)\frac{r}{r_o}\right\rangle_V} \sim \overline{\langle \nabla^2 \boldsymbol{u} \cdot \boldsymbol{e}_r \rangle_V} \sim \frac{Re_{pol}}{\mathcal{L}_h^2}. \tag{3.17}$$

Likewise, the average of the heat equation (2.4) leads to

$$Re_{pol}\frac{\Delta_b\Theta}{\lambda_b} \sim \frac{\overline{\langle T \rangle_V}}{Pr\mathcal{L}_h^2}. \tag{3.18}$$

Finally, a relationship between $\overline{\langle T \rangle_V}$ and $\overline{\langle \xi \rangle_V}$ is expressed by means of the flux ratio γ

$$\overline{\langle \xi \rangle_V} \sim \frac{Le|Ra_T|}{\gamma Ra_\xi}\overline{\langle T \rangle_V}, \tag{3.19}$$

which, in light of (2.19), assumes implicitly that the radial velocity correlates well with thermal and chemical fluctuations. Upon combining (3.17)–(3.19), we obtain

$$\mathcal{L}_h^{-4} \sim (\gamma^{-1} - 1)|Ra_T|\frac{\Delta_b\Theta}{\lambda_b}. \tag{3.20}$$

The bulk temperature gradient $\Delta_b\Theta/\lambda_b$ aside, this expression is equivalent to that proposed by Taylor & Bucens (1989) in the discussion of their experimental results. Figure 7(*b*) shows $\mathcal{L}_h$ as a function of $|Ra_T|(\gamma^{-1} - 1)$. The extra factor $(\gamma^{-1} - 1)$
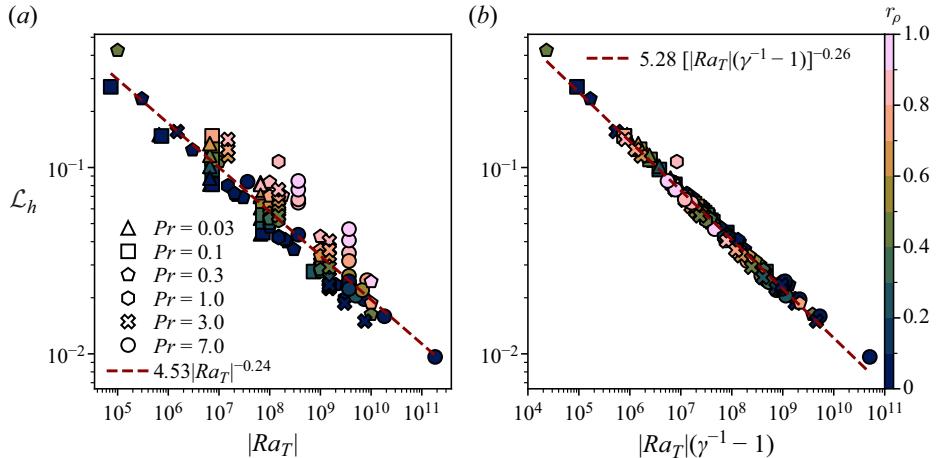
Figure 7. (a) Horizontal length scale $\mathcal{L}_h$ (2.21) as a function of $|Ra_T|$. (b) Value of $\mathcal{L}_h$ as a function of $|Ra_T|(\gamma^{-1} - 1)$. In both panels, the dashed lines correspond to power law fits.

removes the dispersion observed in figure 7(a). A least-squares fit of $\log_{10}(\mathcal{L}_h)$ vs $\log_{10}[|Ra_T|(\gamma^{-1} - 1)]$ leads to

$$\mathcal{L}_h = 5.28 \left[(\gamma^{-1} - 1)|Ra_T| \right]^{-0.26}. \tag{3.21}$$

The exponent of $|Ra_T|$ remains close to the value of -0.25 proposed by Stern (1960). In order to assess the effect of the $\Delta_b \Theta / \lambda_b$ term, we introduce the misfit

$$\chi_y^2 = \sqrt{\frac{1}{N} \sum_{i=1}^{N} \left| \frac{\tilde{y}_i - y_i}{y_i} \right|^2}, \tag{3.22}$$

where N is the number of simulations, y_i is the ith measured value of $\log_{10}(\mathcal{L}_h)$ and $\tilde{y}_i$ its prediction by the least-squares fit of interest. In the absence of a correction factor, recall (3.16), we obtain $\chi_y^2 = 0.091$. With the full correction (3.20), $\chi_y^2 = 0.023$, which amounts to a fourfold reduction. The misfit increases by a modest amount to 0.025 if we omit the factor $\Delta_b \Theta / \lambda_b$ in (3.20). It thus appears reasonable to ignore that factor for the sake of parsimony. In the remainder of this study, we will therefore adhere to

$$\mathcal{L}_h^4 \sim \frac{\gamma}{1 - \gamma} |Ra_T|^{-1}. \tag{3.23}$$

Following the idea of Schmitt (1979b), we now examine whether the average spherical harmonic degree ℓ_h of fingers in developed convection relates to the degree of the fastest growing mode, ℓ_{FG}. Linearisation of the system (2.2)–(2.5) is conducted by considering small perturbations of the poloidal scalar W, temperature T and composition ξ. Performing a spherical harmonic expansion of these variables leads to equations decoupled in harmonic degree ℓ and independent of the spherical harmonic order m. We use the ansatz

$$[W_\ell, T_\ell, \xi_\ell](t, r) = [\widehat{W_\ell}, \widehat{T_\ell}, \widehat{\xi_\ell}](r) \exp(\tau_\ell t), \tag{3.24}$$

where $[\widehat{W_\ell}, \widehat{T_\ell}, \widehat{\xi_\ell}]$ are the radial shape functions of the perturbation of degree ℓ. Focusing on the real-valued eigenvalues τ_ℓ relevant to the fingering instability, we obtain the

988 A18-18
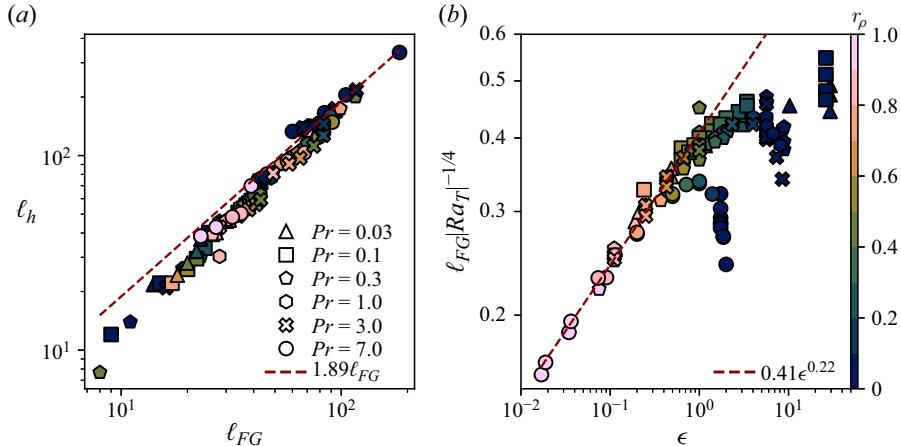
Figure 8. (*a*) Mean spherical harmonic degree ℓ_h as a function of the degree of the fastest growing mode ℓ_{FG}; the dashed line shows the result of the linear regression. (*b*) Most linearly unstable degree $\ell_{FG}|Ra_T|^{-1/4}$ as a function of the supercriticality parameter ϵ. The dashed line in panel (*a*) corresponds to a linear fit forced over the entire dataset, yielding a prefactor equal to 1.89, while the best fit in panel (*b*) was obtained from the simulations with $\epsilon < 0.5$.

generalised eigenvalue problem

$$\mathcal{A}_\ell \boldsymbol{X}_\ell = \tau_\ell \mathcal{B}_\ell \boldsymbol{X}_\ell, \tag{3.25}$$

where $\mathcal{A}_\ell$ and $\mathcal{B}_\ell$ are real dense matrices, $\boldsymbol{X}_\ell \equiv [W_\ell, T_\ell, \xi_\ell]^{\mathrm{T}}$ is the state vector and we understand that each eigenvalue depends on ℓ, Ra_T, Ra_ξ, Pr and Le. We resort to the Linear Solver Builder (LSB) package developed by Valdettaro *et al.* (2007) to determine the harmonic degree ℓ_{FG} of the fastest growing mode which corresponds to $\ell_{FG} = \arg\max_\ell \tau_\ell$ for any given set-up of the numerical dataset.

Figure 8(*a*) shows ℓ_h as a function of ℓ_{FG}. To first order, ℓ_h grows almost linearly with ℓ_{FG} and the proportionality coefficient linking the two harmonic degrees seems to weakly depend on the input parameters. We find that ℓ_h is consistently greater than ℓ_{FG}. The linear fit $\ell_h = 1.89\,\ell_{FG}$ is shown as a dashed line in figure 8(*a*), and is overall in agreement with the simulations. Significant departures occur for $\ell_{FG} < 30$, as the least turbulent simulations tend towards verifying $\ell_h = \ell_{FG}$ (see e.g. the pentagon at the bottom left of figure 8*a*). Far from onset, a large number of modes are excited and the broadening of the spectra noticeable in figure 3(*d*) reflects the nonlinear interaction of theses modes.

The fastest growing modes can be expanded in powers of a supercriticality parameter ϵ which quantifies the distance to onset of fingering convection

$$\epsilon = \frac{Ra_\xi - |Ra_T|}{|Ra_T|} = \frac{Le}{R_\rho} - 1. \tag{3.26}$$

For finite Prandtl numbers, the first-order contribution reads (e.g. Schmitt 1979*b*; Stern & Radko 1998; Radko 2010)

$$\ell_{FG}^4 \sim \epsilon|Ra_T|, \tag{3.27}$$

in the limit of vanishing ϵ. Figure 8(*b*) shows the spherical harmonic degree of the fastest growing mode $\ell_{FG}|Ra_T|^{-1/4}$ as a function of the distance to onset ϵ. The best fit to the data reveals a good agreement with the expected theoretical scaling whenever $\epsilon \ll 1$. Significant departures appear beyond $\epsilon \approx 0.5$, indicating the limit of validity of the scaling (3.27).
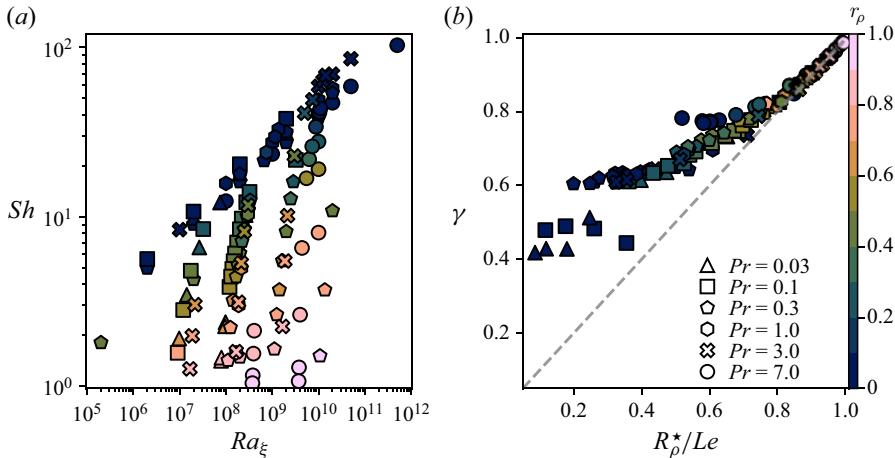
Figure 9. (*a*) Sherwood number *Sh* as a function of Ra_ξ. (*b*) Flux ratio γ as a function of $R_\rho^\star/Le$. The dashed line corresponds to the first bisector $\gamma = R_\rho^\star/Le$.

We hence retain from figure 8 that the hypothesis put forward by Schmitt (1979*b*) – i.e. that the finger width relates to the horizontal size of the fastest growing mode – works better for weakly nonlinear models, i.e. when $\epsilon \ll 1$. This observation will later be used to derive scaling laws for weakly nonlinear fingering convection.

3.5. *Scaling laws for transport*

We now aim at deriving integral scaling laws for the transport of composition and heat, and for the mean vertical velocity.

Figure 9(*a*) shows *Sh* as a function of Ra_ξ, and two trends emerge: first, at any given Ra_ξ, numerical models with $r_\rho < 0.2$ (dark blue symbols) provide an effective upper bound for the transport of chemical composition. This upper bound of the Sherwood number *Sh* grows with Ra_ξ according to a power law that appears almost independent of *Pr*. Second, close to onset ($r_\rho \simeq 1$), simulations are organised along branches representative of a dependency of *Sh* on Ra_ξ much steeper than the one of the effective upper bound. Each branch corresponds to fixed values of Ra_T, *Pr*, and *Le*, and gradually tapers off to the $r_\rho \ll 1$ trend as the value of r_ρ decreases along the branch. This prompts us to analyse the regimes $r_\rho \simeq 1$ and $r_\rho \ll 1$ separately.

It is also informative to inspect the variations of the turbulent flux ratio γ, as defined by (2.19), in both limits. Figure 9(*b*) shows γ against $R_\rho^\star/Le$. When $r_\rho \ll 1$, γ substantially deviates from $R_\rho^\star/Le$ and gradually saturates around values which decrease upon increasing the Lewis number: simulations with $Le = 3$, $Pr = 7$ (circles) saturate at $\gamma \approx 0.8$, while those with $Pr \leq 1$ (pentagons, hexagons, squares and triangles) gradually tapper off around values of 0.6 and 0.4 for $Le = 10$ and $Le \geq 30$, respectively. The series of simulations with $Pr = 7$ (circles) seems to suggest that the $\gamma \approx 0.8$ plateau may actually precede an increase at even lower values of $R_\rho^\star/Le$, a trend predicted by Kunze (1987) in the limit of $Pr, Le \gg 1$. In contrast, close to onset, the flux ratio is well described by $R_\rho^\star/Le$

$$\gamma \approx \frac{R_\rho^\star}{Le}, \tag{3.28}$$

a behaviour consistent with the arguments put forward by Schmitt (1979*b*).

988 A18-20

3.5.1. *The $r_\rho \simeq 1$ regime*

We shall start our analysis by investigating the weakly nonlinear regime characterised by small values of the supercriticality parameter ϵ defined above in (3.26). In the limit where $\gamma \approx R_\rho^\star / Le$, the scaling law obtained for the finger width (3.20) can be rewritten by breaking down the mean radial profiles into a sum of the conducting state and fluctuations. This yields

$$\mathcal{L}_h^{-4} \sim |Ra_T| \left[\frac{Le}{R_\rho} \left(1 + \frac{\Delta_b \Xi'}{\lambda_b} \right) - 1 - \frac{\Delta_b \Theta'}{\lambda_b} \right], \tag{3.29}$$

where we have assumed that $|\mathrm{d}\xi_c/\mathrm{d}r| = \mathrm{d}T_c/\mathrm{d}r \approx 1$. Now, based on our previous findings that the finger width is well accounted for by the horizontal size of the fastest growing mode whenever $\epsilon \ll 1$ (recall figure 8), we have

$$|Ra_T| \left[\frac{Le}{R_\rho} \left(1 + \frac{\Delta_b \Xi'}{\lambda_b} \right) - 1 - \frac{\Delta_b \Theta'}{\lambda_b} \right] \sim |Ra_T| \left(\frac{Le}{R_\rho} - 1 \right), \tag{3.30}$$

which leads to

$$\frac{\Delta_b \Theta'}{\lambda_b} \sim \frac{\epsilon}{Le^2 \gamma^{-1} - 1}, \tag{3.31}$$

in which the ratio of $\Delta_b \Xi' / \Delta_b \Theta'$ has been estimated using (3.9).

Making use of the definitions (2.22a–c) then allows us to relate the ratio $\Delta_b \Theta' / \lambda_b$ to its boundary layer counterpart, namely

$$\frac{\Delta_b \Theta'}{\lambda_b} = \frac{\Delta_o \Theta'}{\lambda_o} \frac{\lambda_o + \lambda_i (\Delta_i \Theta' / \Delta_o \Theta')}{1 - \lambda_i - \lambda_o} \approx \frac{\Delta_o \Theta'}{\lambda_o} \lambda_o [1 + (r_i/r_o)^{-3/2}], \tag{3.32}$$

where the latter equality has been derived using our previous findings regarding the boundary layer asymmetry (3.4)–(3.5). Noting that $Nu - 1 \approx (r_o/r_i) \Delta_o \Theta' / \lambda_o$ and substituting the above expression in (3.31) yields

$$Nu - 1 \sim f(r_i/r_o) \lambda_o^{-1} \frac{\epsilon}{Le^2 \gamma^{-1} - 1}, \tag{3.33}$$

where $f(r_i/r_o) = (r_i/r_o)^{-1} [1 + (r_i/r_o)^{-3/2}]^{-1}$ accounts for the dependence on the radius ratio r_i/r_o inherent in the spherical-shell geometry. Beside these geometrical factors, this expression is strictly equivalent to (5.10) derived by Radko & Stern (2000) in bounded Cartesian domains under the assumption of tall laminar fingers in the fluid bulk.

The end of the derivation, however, differs from Radko & Stern (2000), in that they consider a boundary layer model where the buoyancy term is retained, while we have shown earlier that the compositional boundary layers rather adhere to the Prandtl–Blasius model (see (3.12) and figure 6).

To eliminate the Péclet number Pe in (3.12), one can simply assume that viscous dissipation is well approximated by $D_\nu \sim (Re_{pol}/\mathcal{L}_h)^2$. The power balance (2.17) (see also Appendix B) then directly yields

$$Pe \sim \mathcal{L}_h |Ra_T|^{1/2} Le (Nu - 1)^{1/2} (\gamma^{-1} - 1)^{1/2}. \tag{3.34}$$

Hence, combining (3.12), (3.33) and (3.34), the scaling relation for $Nu - 1$ reads

$$Nu - 1 \sim \frac{\epsilon^{6/5} |Ra_T|^{3/10} Le^{2/5} (\gamma^{-1} - 1)^{3/10}}{(\gamma^{-1} Le^2 - 1)^{6/5}}, \tag{3.35}$$

where the order-one geometrical factors have been omitted. To end up with a scaling relation which solely depends on control quantities, one can further approximate the
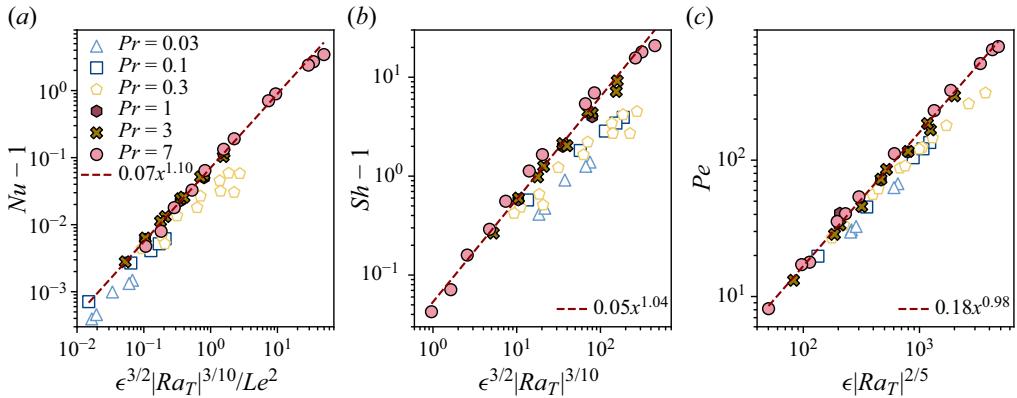
Figure 10. (*a*) Vertical convective transport of heat $Nu - 1$ as a function of the theoretical weakly nonlinear scaling (3.36) for all the simulations with $\epsilon < 1$. (*b*) Vertical convective transport of composition as a function of the scaling (3.37). (*c*) Convective velocity as a function of the scaling (3.38). The dashed lines correspond to the best fits obtained for the numerical simulations with $Pr \geq 1$ and $\epsilon < 0.5$.

flux ratio by $\gamma \approx R_\rho/Le$, or equivalently assume that $\gamma^{-1} - 1 \approx \epsilon$. Noting that this latter assumption is more restrictive than (3.28) and that $R_\rho/Le = 1 - \epsilon$, the first-order contribution leads to

$$Nu - 1 \sim \epsilon^{3/2}|Ra_T|^{3/10}Le^{-2}, \tag{3.36}$$

while the corresponding scaling behaviour for $Sh - 1$ then reads

$$Sh - 1 \approx Le^2(Nu - 1) \sim \epsilon^{3/2}|Ra_T|^{3/10}. \tag{3.37}$$

The scaling for the vertical velocity (3.34) then becomes

$$Pe \sim \epsilon|Ra_T|^{2/5}. \tag{3.38}$$

Equations (3.36)–(3.38) form the weakly nonlinear scaling behaviour for bounded fingering convection. The scaling exponents on the supercriticality parameter ϵ differ from those derived by Radko & Stern (2000) due to different boundary layer models. Figure 10 shows an evaluation of these predictive scaling laws for the 47 simulations with $\epsilon < 1$. Among those, the 25 simulations with $Pr \geq 1$ are reasonably well accounted for by the weakly nonlinear laws. Best fits using the 22 simulations with $\epsilon < 0.5$ yield scaling exponents of ≈ 1.1 for the heat and composition transport, moderately larger than the expected slope of one, while the vertical velocity follows an exponent closer to unity. In contrast, the remaining 22 simulations with $Pr < 1$ are more scattered, they significantly depart from the asymptotic laws and seem to demand an extra dependence on the Prandtl number. This is particularly obvious for the scaling of the Sherwood number shown in figure 10(*b*).

The previous derivation rests on several assumptions that become questionable in the limit of small Prandtl numbers. Among the most likely shortcomings, one can think of: (i) the approximation of the flux ratio by $\gamma \approx R_\rho/Le$ getting more uncertain on decreasing Pr; (ii) the relation between the finger width and the size of the fastest growing mode breaking down at low Pr or involving a more intricate dependence on ϵ (Schmitt 1979*b*; Radko 2010); and (iii) inertia becoming sizeable, thus invalidating the laminar tall finger hypothesis. All in all, these additional hurdles hamper the derivation of predictive scaling laws for bounded domains that would hold in the small Prandtl number limit.

For the purpose of comparison with the local unbounded computations by Brown *et al.* (2013) when $Pr < 1$, we nevertheless show in Appendix C that adjusted diagnostics which incorporate the modification of the background profiles into account can be described by simple polynomials fits on Pr and $\epsilon^\star/Le$, where $\epsilon^\star = Le/R_\rho^\star - 1$.

3.5.2. *The $r_\rho \ll 1$ regime*

Turning our attention to the second limit, we retain arbitrarily those 41 simulations with $r_\rho < 0.1$, which cover all values of Pr from 0.03 to 7.

Figure 11(*a*) shows $Sh - 1$ versus Ra_ξ for these simulations, alongside the 31 bounded Cartesian simulations of Yang *et al.* (2016) that satisfy $r_\rho > 0$. A least-squares fit of $Sh - 1$ as a function of Ra_ξ yields $Sh - 1 \sim Ra_\xi^{0.27}$ for our dataset and $Sh - 1 \sim Ra_\xi^{0.31}$ for that of Yang *et al.* (2016). The extension of the theory of Grossmann & Lohse (2000) for Rayleigh–Bénard convection to fingering convection by Yang *et al.* (2015) predicts $Sh \sim Ra_\xi^{1/3}$ in the $Ra_\xi \gg 1$ limit when dissipation occurs in the fluid bulk. However, for the range of Ra_ξ covered in this study, a non-negligible fraction of dissipation is expected to happen within the boundary layers. In addition, our mixture of Prandtl numbers above and below unity may result in superimposed transport regimes. As such, the smaller value of the scaling exponent, as well as the larger spread of the data, compared with those of Yang *et al.* (2016) over a comparable range of Ra_ξ, are not surprising: Yang *et al.* (2016) consider a single combination of parameters ($Pr = 7$, $Le = 100$) that makes it possible to reach values of r_ρ smaller than ours. We only retained the simulations by Yang *et al.* (2016) that satisfied the criterion $r_\rho > 0$, *viz.* $R_\rho > 1$; yet fingers in their case remain stable down to $R_\rho \approx 0.1$, where the scaling $Sh - 1 \sim Ra_\xi^{0.31}$ still holds (not shown). Finally, we note that the chemical transport for the $Pr < 1$ data shown in figure 11(*a*) also follows the $Ra_\xi^{0.27}$ law, in stark contrast to the predictions of a constant Sh for a fixed (Le, Pr) pair derived by Brown *et al.* (2013) in unbounded planar models with $Pr \ll 1$.

Using (3.34), the definition of the flux ratio (2.19) and the scaling for $Sh - 1$ with Ra_ξ just discussed, and assuming that $[\gamma(1 - \gamma)]^{1/2}$ can be considered constant, we expect

$$Pe \sim Ra_\xi^{2/3}|Ra_T|^{-1/4}, \tag{3.39}$$

in the asymptotic $Sh \sim Ra_\xi^{1/3}$ regime. Figure 11(*b*) shows $Pe|Ra_T|^{1/4}$ as a function of Ra_ξ for our dataset and that of Yang *et al.* (2016). Least-squares fits yield scaling exponents that are remarkably close to 2/3 for both subsets, and a spread of our data along the best-fit line less pronounced than in figure 11(*a*). The difference in the prefactors of the best-fit lines describing our dataset and that of Yang *et al.* (2016) can be ascribed to the differences in model set-ups (Cartesian vs spherical geometry and constant gravity vs gravity increasing with *r*).

A few comments are in order with regard to (3.39): operating at fixed $Le = 100$, Yang *et al.* (2016) propose a scaling for the vertical velocity in terms of the Reynolds number Re

$$Re \propto R_\rho^{-1/4}Ra_\xi^{1/2} \propto Ra_\xi^{3/4}|Ra_T|^{-1/4}Le^{-1/4}, \tag{3.40}$$

which, in light of their figure 4(*b*), does not yield as good an agreement with their data as the scaling proposed here for *Pe*, and shown in figure 11(*b*). Expressing our proposed
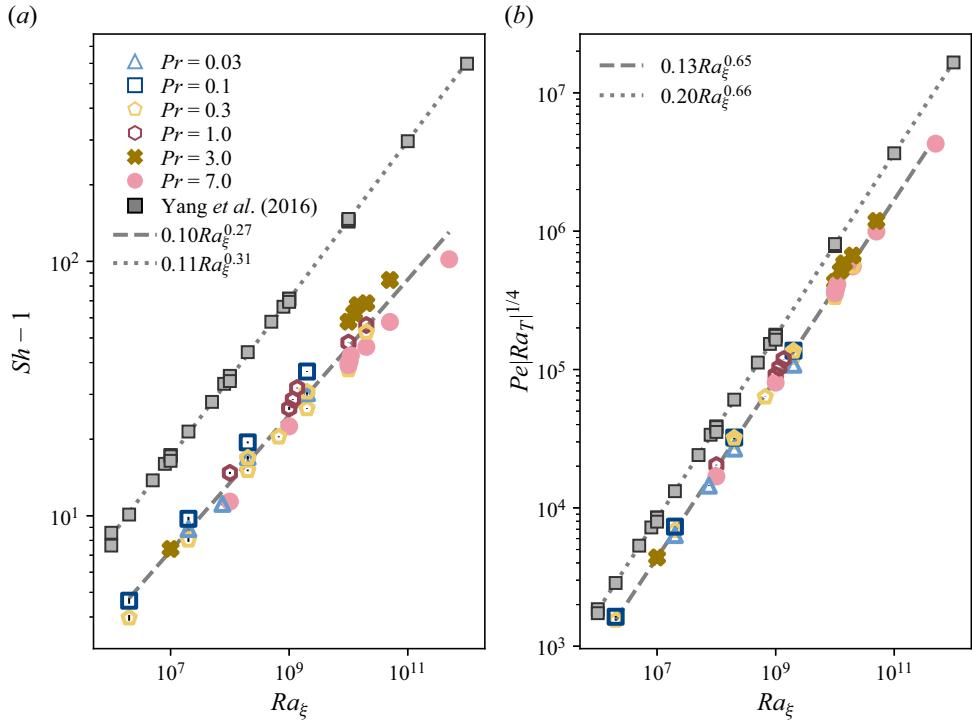
Figure 11. (*a*) Value of $Sh - 1$ as a function of Ra_ξ for our numerical simulations with $r_\rho < 0.1$ alongside the data from Yang *et al.* (2016) that fulfil $R_\rho > 1$. (*b*) Value of $Pe|Ra_T|^{1/4}$ as a function of Ra_ξ. In both panels, dashed and dotted lines correspond to least-square fits to our data and to those of Yang *et al.* (2016), respectively.

scaling in terms of Re gives

$$Re \sim Ra_\xi^{2/3} |Ra_T|^{-1/4} Sc^{-1}, \tag{3.41}$$

which exhibits a slightly smaller dependency on Ra_ξ than the one put forward by Yang *et al.* (2016), and does a better job of fitting their data (not shown). Yang *et al.* (2016) acknowledged that additional dependency on Pr and Sc (or Le) might occur since only one combination is considered in their study, in particular when discussing the scaling $Re \sim Ra_\xi |Ra_T|^{-1/2}$ proposed by Hage & Tilgner (2010) based on their experimental data with $Pr \approx 9$ and $Sc \approx 2200$. The exponents found by Hage & Tilgner (2010) are markedly different from the ones inferred from our analysis. It should be noted, however, that their experimental data cover a region of parameter space where the density ratio is mostly smaller than unity, in which fingers can be gradually replaced by large-scale convection. Under those circumstances, the hypothesis that dissipation can be expressed by $D_\nu \sim (Re_{pol}/\mathcal{L}_h)^2$, with $\mathcal{L}_h$ the typical finger width, breaks down.

4. Toroidal jets

In a substantial subset of simulations, a secondary instability develops on top of the radially oriented fingers, in the form of large-scale horizontal flows. Jets formation has been observed in 2-D unbounded simulations by Radko (2010) and Garaud & Brummell (2015) for $Pr < 1$ fluids. More recently, Yang *et al.* (2016) reported the formation of

alternating zonal jets in a 3-D bounded geometry with $Pr = 7$ and $Le = 100$ when $Ra_\xi > 10^{10}$. The purpose of this section is to characterise the spatial and temporal distributions of jets forming in spherical-shell fingering convection.

4.1. *Flow morphology*

Figure 12 shows 3-D renderings of snapshots of the azimuthal velocity for four selected numerical simulations. Upper panels (*a,b*) correspond to simulations which share the same parameters $Pr = 0.3$, $|Ra_T| = 10^8$, $Le = 10$ and only differ in the values of the density ratio R_ρ, $R_\rho = 6$ in figure 12(*a*) and $R_\rho = 5$ in figure 12(*b*). To highlight the spatial distribution of the toroidal jet, figure 12(*a,b*) also shows streamlines of the large-scale component of the flow truncated at spherical harmonic degree $\ell = 7$. In both simulations, the large-scale component of the flow takes the form of one single jet which reaches its maximum amplitude around mid-shell (red thick streamline tubes). We note in passing that the 22 simulations with $Pr < 1$ of our dataset which develop toroidal jets systematically feature one singly oriented jet that spans most of the spherical-shell volume. The absence of background rotation precludes the existence of a preferential direction in the domain, and the axis of symmetry of the jet has the freedom to evolve over time. In panel (*a*), the toroidal Reynolds number reaches 24, comparable to the velocity of the fingers $Re_{pol} = 41$. The fivefold increase of the buoyancy power between figures 12(*a*) and 12(*b*) results in a stronger jet, which now reaches $Re_{tor} = 87$, a value slightly larger than the finger velocity $Re_{pol} = 77$. Interestingly, a further decrease of R_ρ to 3.25 (not shown) results in the decrease of Re_{tor} and the eventual demise of toroidal jets for lower R_ρ. This is suggestive of a minimum threshold value of R_ρ favourable to trigger jet formation.

The numerical models shown in the lower panels (*c,d*) of figure 12 share the same values of $Pr = 3$, $Le = 10$ and $R_\rho = 1.5$ but differ in their values of Ra_ξ and Ra_T. In the case shown in figure 12(*c*) with $Ra_\xi = 10^{10}$, faint multiple jets of alternated directions develop. Their amplitudes remain, however, weak compared with the finger velocity with $Re_{tor} = 14$ and $Re_{pol} = 72$. As can be seen in the equatorial plane (colatitude $\theta = \pi/2$), jets do not exhibit a perfectly coherent concentric nature over the entire fluid volume but rather adopt a spiralling structure with significant amplitude variations. As shown in figure 12(*d*), an increase of the convective driving to $Ra_\xi = 5 \times 10^{10}$ goes along with the formation of a stack of 6 alternated jets. Although their amplitude remains smaller than the fingering velocity ($Re_{tor} = 45$ and $Re_{pol} = 134$), toroidal jets now adopt a quasi-concentric structure with well-defined boundaries. This latter configuration is reminiscent of the simulations of Yang *et al.* (2016), who also report the formation of multiple jets in local Cartesian numerical models with $Pr = 7$ and $R_\rho = 1.6$ when $Ra_\xi \geq 10^{11}$. Similarly to Yang *et al.* (2016), we also observe that toroidal jets develop in configurations with $Pr \geq 1$ for small values of R_ρ and sufficiently large values of Ra_ξ. Critical values of those parameters required to trigger jet formation are further discussed below.

4.2. *Time evolution*

To illustrate the growth of toroidal jets, we show in figure 13 the time evolution of the poloidal and toroidal kinetic energy alongside kinetic energy spectra for two illustrative numerical simulations which feature jets with $Ra_T = -10^8$, $Pr = 0.3$, $Le = 10$ and $R_\rho = 4$ (upper panels, simulation 53 in table 3) and $Ra_T = -1.5 \times 10^8$, $Pr = 1$, $Le = 10$ and $R_\rho = 1.3$ (lower panels, simulation 72). For the case with $Pr = 0.3$ (figure 13a), $E_{k,tor}$ is initially 25 times weaker than $E_{k,pol}$. Beyond $t \approx 4.2$, $E_{k,tor}$ grows exponentially over
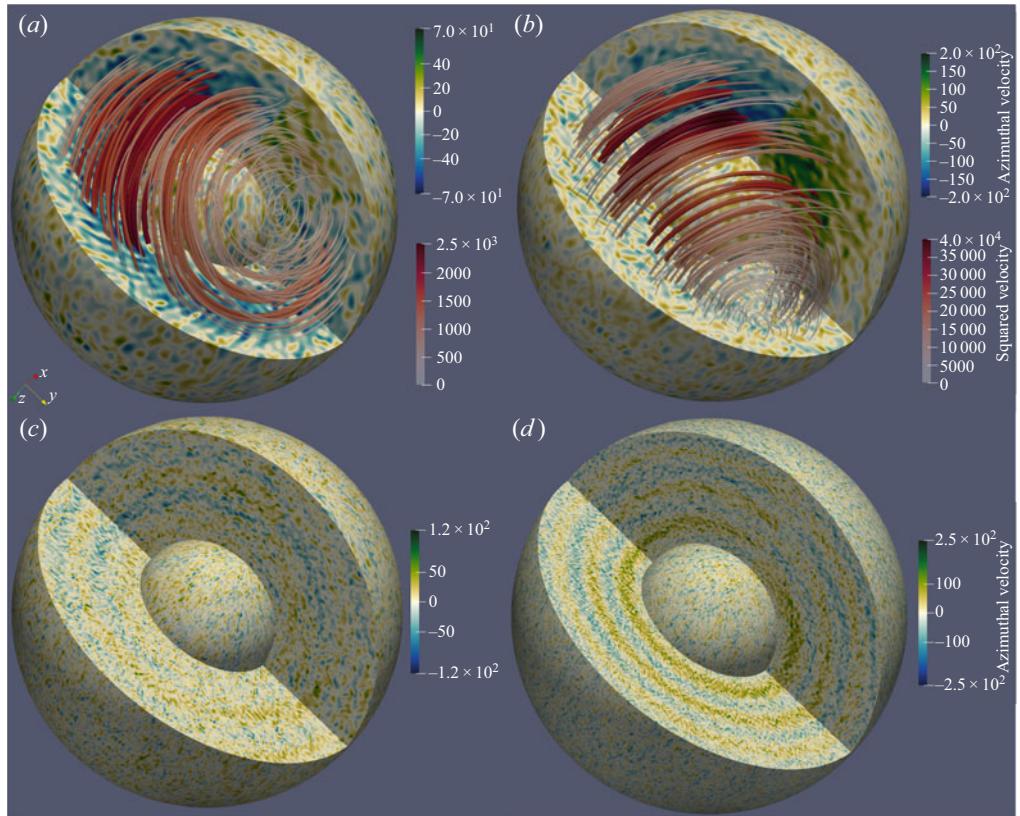
Figure 12. Three-dimensional renderings of the instantaneous longitudinal velocity u_φ for four simulations. The inner and outer spherical surfaces correspond to $r_i + 0.03$ and $r_o - 0.04$. (*a,b*) The two simulations share $Pr = 0.3$, $Le = 10$ and $Ra_T = -10^8$ (simulations 57 and 53 in table 3). The value of R_ρ is equal to 6 in (*a*) and 4 in (*b*). Streamlines correspond to the large-scale component of the flow, truncated at a spherical harmonic degree $\ell = 7$. The width and the colour of the streamlines vary according to the local squared velocity. The two simulations on the bottom row (*c,d*) share $Pr = 3$, $Le = 10$ and $R_\rho = 1.5$ (simulations 84 and 80). The simulation shown in (*c*) has $(Ra_T, Ra_\xi) = (-1.5 \times 10^9, 10^{10})$, while that shown in (*d*) has $(Ra_T, Ra_\xi) = (-7.5 \times 10^9, 5 \times 10^{10})$.

approximately one viscous diffusion time and saturates at a value which exceeds $E_{k,pol}$. In contrast, the case with $Pr = 1$ (figure 13*c*) exhibits a much slower growth of the toroidal energy: $E_{k,tor}$ gains one order of magnitude in more than 3 viscous diffusion times. At the saturation of the instability around $t \approx 9$, $E_{k,tor}$ remains a factor 3 smaller than $E_{k,pol}$ in this case. The growth of the toroidal energy goes along with the formation of one or several large-scale jets (see figure 12), which are clearly visible in the kinetic energy spectra. Figures 13(*b*)–13(*d*) show the kinetic energy spectra as a function of the spherical harmonic degree at three different times: before the start of the instability (blue lines), during the exponential growth of the jets (yellow lines) and at the saturation of the instability (red lines). In both cases, the initial spectral distributions of energy are typical of fingering convection with a well-defined maximum around the average spherical harmonic degree ℓ_h which corresponds to the mean horizontal size of the fingers (recall figure 3*d*). The growth of $E_{k,tor}$ manifests itself in an increase of several orders of magnitude of the energy at the largest scale $\ell = 1$. In the saturated state, the kinetic energy spectra now reach their maxima at $\ell = 1$ and feature a secondary peak of smaller amplitude at $\ell = 3$.
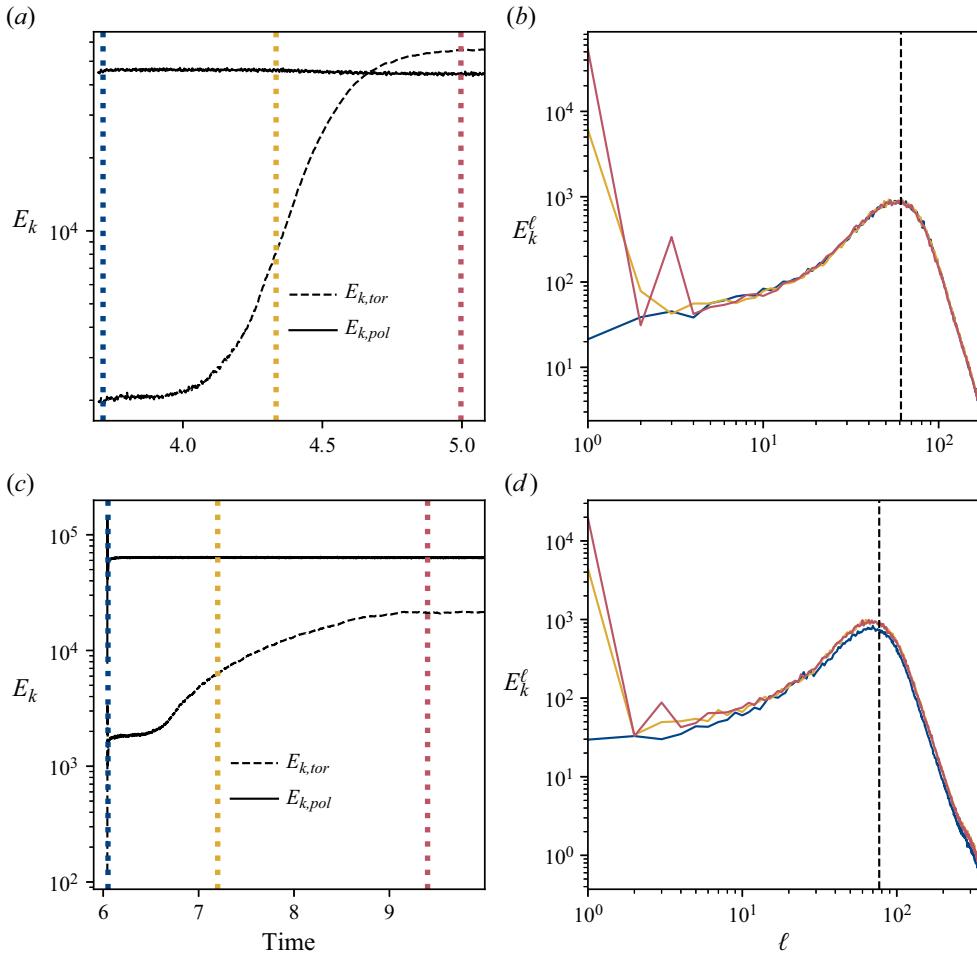
Figure 13. (a,c) Time evolution of the poloidal (toroidal) kinetic energy $E_{k,pol}$ ($E_{k,tor}$). (b,d) Kinetic energy spectra as a function of the spherical harmonic degree ℓ shown at three distinct times which correspond to the vertical dotted lines in the left panels. Panels (a,b) correspond to a simulation with $Ra_T = -10^8$, $Pr = 0.3$, $Le = 10$ and $R_\rho = 4$ (simulation 53 in table 3), while panels (c,d) correspond to a simulation with $Ra_T = -1.5 \times 10^8$, $Pr = 1$, $Le = 10$ and $R_\rho = 1.3$ (simulation 72). In panels (b,d), the vertical lines correspond to ℓ_h.

The toroidal energy at degree $\ell = 1$ $E_{k,tor}^1$ is hence a good measure of the energy contained in the jets. Beyond $\ell \gtrsim 6$, the spectra remain quite similar to their distribution prior to the onset of jet formation. This indicates a limited feedback of the growth of the jets on the horizontal size of the fingers.

To further characterise the physical parameters propitious to the formation of toroidal jets, figure 14 shows the time evolution of the toroidal kinetic energy contained in the $\ell = 1$ degree at a given radius around $\approx 0.8\,r_o$ for two series of simulations. Figure 14(a) shows simulations with $Ra_T = -10^8$, $Pr = 0.3$, $Le = 10$ and increasing $r_\rho^\star$. For the case with the smallest $r_\rho^\star = 0.47$, jets do not form since the toroidal energy at $\ell = 1$ oscillates but does not grow over time. For $r_\rho^\star \geq 0.5$, $E_{k,tor}^1$ grows exponentially over one viscous diffusion time before reaching saturation. The amplitude of $E_{k,tor}^1$ reaches its maximum

(*a*)

(*b*)
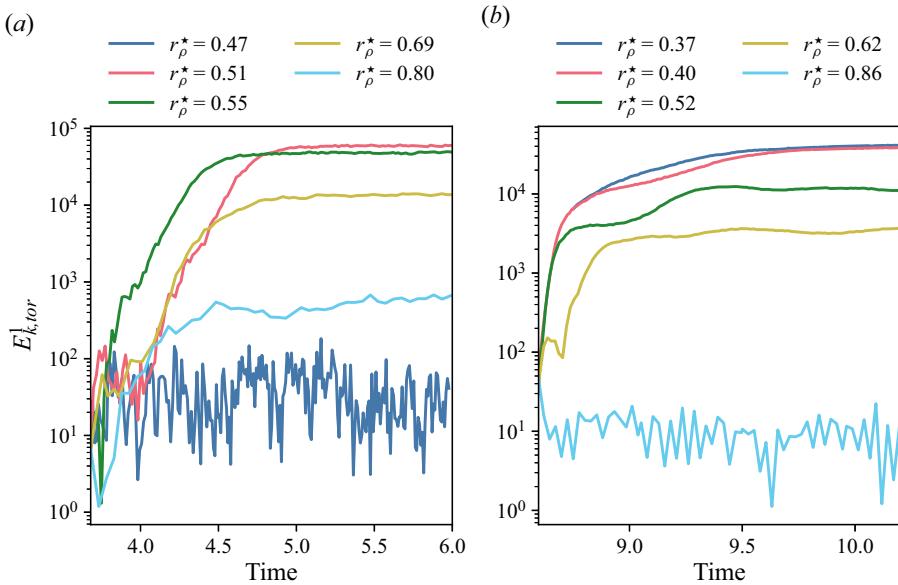
Figure 14. (*a*) Time evolution of the toroidal kinetic energy contained in the $\ell = 1$ harmonic degree at a given radius r for simulations with $Ra_T = -10^8$, $Pr = 0.3$, $Le = 10$ and a varying $r_\rho^\star$ (simulations 50, 52, 53, 56 and 58 in table 3). For all of them but one, $r = 0.793\,r_o$. The simulation with $r_\rho^\star = 0.40$ is shown for $r = 0.858\,ro$. (*b*) Same for simulations with $Ra_T = -3.66 \times 10^9$, $Pr = 7$, $Le = 3$ (simulations 106, 107, 109, 110 and 112) and $r = 0.785\,r_o$.

for the cases with $r_\rho^\star \approx 0.5$–0.55 and then decreases for larger values. The growth rate of the instability remains, however, markedly similar over the range of $r_\rho^\star$ considered here. The simulation with $r_\rho^\star = 0.80$ is the last one of the series that features jets. For the models with $Pr = 0.3$, jets hence only develop on a bounded interval of $r_\rho^\star$. Figure 14(*b*) shows simulations with $Ra_T = -3.66 \times 10^9$, $Pr = 7$ and $Le = 3$. All the numerical models with $r_\rho^\star < 0.86$ present an exponential growth of $E_{k,tor}^1$ with once again comparable growth rates. In contrast to the $Pr < 1$ cases, jets appear to form below a threshold value of $r_\rho^\star$, while displaying a monotonic trend: the lower $r_\rho^\star$ below the threshold, the stronger the jets.

Once the toroidal jets have saturated, $Pr < 1$ and $Pr \geq 1$ simulations exhibit distinct time evolutions: cases with $Pr < 1$ are dominated by one single jet with a well-defined rotational symmetry with no preferred axis (see figure 12*a*,*b*), while $Pr \geq 1$ cases usually feature a more complex stack of multiple alternated jets with different axes of symmetry. The latter are also more prone to time variations than the former. To illustrate this phenomenon, figure 15 shows the time evolution of the longitudinal average of u_ϕ in the equatorial plane for a simulation with $Pr = 3$, $R_\rho = 1.5$, $Le = 10$ and $Ra_\xi = 2 \times 10^{10}$. For this simulation, the $\ell = 1$ toroidal energy is mostly axisymmetric, and the inspection of the azimuthally averaged velocity thus provides a good insight into the jet dynamics. The zonal flow pattern in the first half of the time series consists of three pairs of alternated jets. Jets are nucleated in the vicinity of the bottom boundary before slowly drifting outwards with a constant speed until reaching the outer boundary after ≈ 0.3 viscous diffusion times. In between, another jet carrying the opposite direction has emerged forming a quasi-periodic behaviour. This oscillatory phenomenon is gradually interrupted beyond $t \approx 6.6$. The mid-shell westward jet then strengthens and widens, while the surrounding

988 A18-28
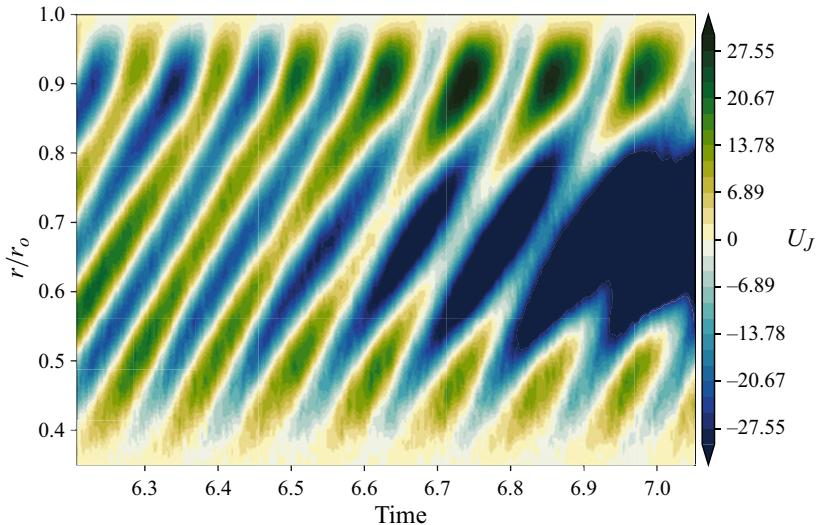
Figure 15. Longitudinal average of the longitudinal velocity in the equatorial plane (colatitude $\theta = \pi/2$), U_J, as a function of radius r and time t. Control parameters for this simulation are $Pr = 3$, $Le = 10$, $Ra_\xi = 2 \times 10^{10}$ and $R_\rho = 1.5$ (simulation 81 in table 3).

eastward jets vanish. The multiple drifting jets therefore transit to a single jet configuration within less than one viscous diffusion time. The long-term stability of the multiple jet configuration when $Pr \geq 1$ is hence in question. Since the jets merging seems to occur on time scales commensurate with the viscous time scale, a systematic survey of the stability of the multiple jet configuration is numerically daunting. We decided to instead focus on a selected subset of multiple jet simulations with $Pr \geq 1$ which were integrated longer to examine the merging phenomenon. As stated above, the 5 multiple jet cases whose integration is too short to assess a possible merger feature an additional 'NS' in the last column of table 3. It is, however, striking to note that all the simulations that have been pursued longer eventually evolve into a single jet configuration; the merging time taking up to twice the viscous diffusion time. This phenomenon is reminiscent of the 2-D numerical models by Xie *et al.* (2019) who also report jets merging over time scales 4 orders of magnitude larger than the thermal diffusion time at the scale of a finger. For comparison purposes, the time integration of the case shown in figure 15 corresponds to roughly 7000 thermal diffusion times at the finger scale.

4.3. *Instability domain*

Jet formation systematically leads to the growth of the toroidal kinetic energy content at the largest scales (recall figure 13). To distinguish jet-producing simulations from the others, we introduce the following empirical criterion:

$$\zeta = \left(1 - \frac{\sum_{\ell=1}^{\ell=5} E_{k,tor}^\ell}{\sum_{\ell=1}^{\ell=11} E_{k,tor}^\ell}\right)^{-1} > 20, \tag{4.1}$$

whose purpose is to reveal the emergence of large-scale toroidal energy, for spherical harmonic degrees ℓ in the range $[\![1, 5]\!]$, using a baseline defined by the spherical harmonic
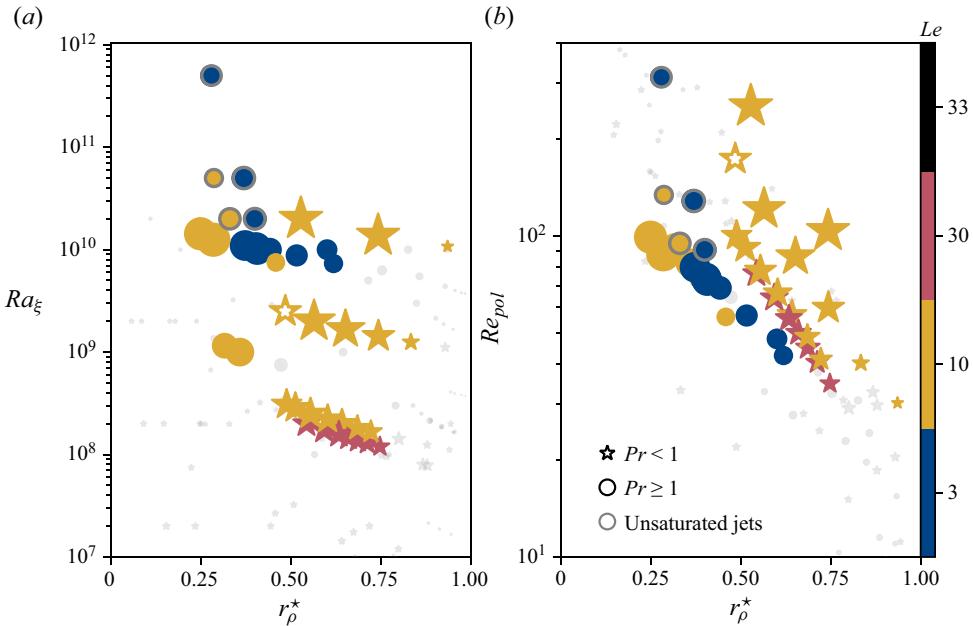
Figure 16. (*a*) Location of the 123 simulations computed in this study in the $r_\rho^\star - Ra_\xi$ plane. (*b*) Same in the $r_\rho^\star - Re_{pol}$ plane. Stars and discs denote $Pr < 1$ and $Pr \geq 1$, respectively. Grey symbols correspond to models without jets. Conversely, symbols corresponding to simulations with single or multiple jets according to the criterion (4.1) are coloured according to the value of the Lewis number *Le*. Symbol size is proportional to Re_{tor}^1/Re_{pol}, where Re_{tor}^1 is the Reynolds number constructed from the spherical harmonic degree $\ell = 1$ component of the toroidal flow. The 5 simulations with jets whose symbol has a grey rim were not integrated for a long enough time to witness the possible merging of their multiple jets, which may lead to an underestimation of Re_{tor}^1/Re_{pol}. The white star with a yellow rim corresponds to the simulation further discussed in figure 19.

degrees ℓ in the range $[\![6, 11]\!]$, whose level is immune to jet formation, see figures 13(*b*) and 13(*d*). The threshold of 20 is arbitrary and enables a clear separation to be made between those simulations producing jets and the others.

Figure 16 shows the location of the 123 simulations in the $r_\rho^\star - Ra_\xi$ (*a*) and $r_\rho^\star - Re_{pol}$ (*b*) planes. In order to highlight the models which develop jets, the coloured symbols in figure 16 correspond to cases with toroidal jets and the symbol size scales to the relative energy content in $E_{k,tor}^1$. Configurations prone to jet formation are only observed beyond $Ra_\xi \approx 10^8$ for $Pr < 1$ and beyond $Ra_\xi \approx 10^9$ for $Pr \geq 1$, which indicates that a minimum level of convective forcing is required to trigger the onset of jet formation. This is in line with the findings of Yang *et al.* (2016), who also found jets forming beyond $Ra_\xi \geq 10^{11}$ in their models with $Pr = 7$, $Le = 100$ and $R_\rho = 1.6$.

For the numerical models with $Pr < 1$ (yellow and red stars), jets form over a bounded domain of $r_\rho^\star$. The instability domain grossly spans $r_\rho^\star \in [0.4, 0.8]$ but also features an additional dependence on Ra_T. The three quasi-horizontal branches of yellow stars correspond to numerical simulations with $|Ra_T| = 10^8$, 10^9 and 10^{10}, respectively. For each value of $|Ra_T|$, the largest relative energy content in the large-scale jets is attained close to the lower boundary of the instability domain. Increasing $|Ra_T|$ goes along with a gradual shift of the instability domain towards larger values of $r_\rho^\star$. Simulations with $Pr = 0.1$ and $Le = 30$ (red stars) feature a smaller instability domain than $Pr = 0.3$, $Le = 10$ (yellow stars). For the lowest $Pr = 0.03$ configurations considered here, not a

single model satisfies the criterion employed to detect jets. We note, however, that two simulations with $Pr = 0.03$ and $r_\rho^\star \approx 0.8$ feature a sizeable increase in $E_{k,tor}^1$, such that $E_{k,tor}^1 \approx 10 E_{k,tor}^2$, yet insufficient to fulfil the criterion. This indicates that the instability domain for jet formation shrinks upon decreasing Pr, with a concomitant decrease of jet amplitude. Jets are hence unlikely to form in the $Pr \ll 1$ regime (Garaud & Brummell 2015).

For the models with $Pr \geq 1$ (disks in figure 16), jets develop for $Ra_\xi \geq 10^9$ for $Pr = 3$ (yellow disks) and for $Ra_\xi \geq 10^{10}$ for $Pr = 7$ (blue disks) for a range of $r_\rho^\star$ which roughly spans [0, 0.5]. At a given convective forcing Ra_ξ, the largest relative jet amplitude seems to correspond to the smallest values of $r_\rho^\star$. Because of the slow merging of the multiple jet configuration when $Pr \geq 1$, their final amplitude is, however, hard to assess for those 5 simulations that have not reached saturation and are represented by symbols with a grey rim in figure 16.

It is clear from figure 16(*a*) that the sole value of Ra_ξ does not provide a reliable criterion for jet formation, since its critical value depends on both Pr and Le. As an attempt to devise a more generic criterion, figure 16(*b*) shows the distribution of simulations in the $r_\rho^\star - Re_{pol}$ plane. Series of simulations with a fixed value of $|Ra_T|$ now define inclined branches, along which the amplitude of Re_{pol} increases upon decreasing $r_\rho^\star$. All the configurations prone to jet formation satisfy $Re_{pol} > 30$. This is of course not a sufficient condition, since, as discussed earlier, the $Pr \lesssim 1$ configurations also demand $r_\rho^\star \in [0.4, 0.8]$, while the $Pr \geq 1$ require $r_\rho^\star < 0.5$ to develop jets. Overall, this stresses the need for a sufficiently vigorous background of fingering convection to trigger the secondary instability leading to jet formation.

To better characterise the mechanism of jet formation, we now focus on one particular model with $Pr = 0.3$, $Le = 10$, $Ra_\xi = 2 \times 10^8$ and $R_\rho = 5$, where only one single jet develops (simulation 55 in table 3). To ease the analysis, the axis of symmetry of the jet has been enforced to perfectly align with the z-axis by imposing a twofold azimuthal symmetry. Figure 17 shows two snapshots of the convective flow close to the equatorial plane prior to the jet formation and at the saturation of the instability. Before the jets start to grow (figure 17*a*), fingers present an almost tubular structure. After almost two viscous diffusion times, a strong jet aligned with the z-axis (colatitude $\theta = 0$) has developed and reaches a velocity which exceeds the radial flow (figure 17*b*). Fingers have lost their vertical structure and are now distorted in the direction of the background shear. This is reminiscent of the analysis by Holyer (1984), who showed that fingering convection is prone to developing secondary instabilities that can be either oscillatory or non-oscillatory. The latter take the form of horizontal motions perpendicular to the axis of the fingers (see her figure 1). This secondary instability shears the initially tubular fingers, while distorted fingers yield a correlation between the convective flow components that can, in turn, feed the shear by Reynolds stress (see Stern & Simeonov 2005, § 3.1). The 2-D numerical models by Shen (1995) with $Pr = 7$, $Le = 100$ and $R_\rho = 2$ showed that this secondary instability saturates once the fingers are disrupted by shear.

In the case of $Pr < 1$ where only one single jet develops, it is always possible to define without loss of generality a local frame $(\boldsymbol{e}_r, \boldsymbol{e}_\vartheta, \boldsymbol{e}_\varphi)$ in which the jets velocity can be expressed along $\boldsymbol{e}_\varphi$ only. The time and azimuthal average of the azimuthal component of the Navier–Stokes equations (2.3) expressed in this frame of reference then yields a balance between Reynolds and viscous stresses given by

$$\frac{1}{r^2} \frac{\partial}{\partial r} \left(r^2 \overline{\langle u_r u_\varphi \rangle_\varphi} \right) + \frac{1}{r \sin \vartheta} \frac{\partial}{\partial \vartheta} \left(\sin \vartheta \overline{\langle u_\vartheta u_\varphi \rangle_\varphi} \right) = \nabla^2 \overline{U_J} - \frac{1}{r^2 \sin^2 \vartheta} \overline{U_J}, \qquad (4.2)$$
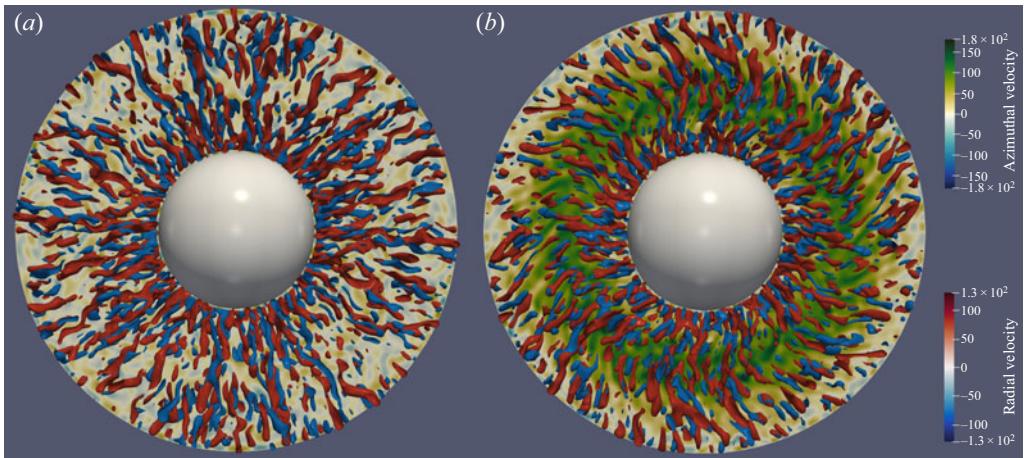
Figure 17. Renderings of the velocity for a numerical model with $Pr = 0.3$, $Le = 10$, $Ra_\xi = 2 \times 10^8$ and $R_\rho = 5$ (simulation 55 in table 3) at $t = 3.98$ (a) and at $t = 5.68$ (b). The equatorial plane shows the azimuthal component of the velocity u_ϕ, while the red and blue surfaces correspond to the iso-levels of the radial velocity $u_r = \pm 80$ in the vicinity of the equatorial plane.

where $\langle \cdots \rangle_\varphi$ denotes an azimuthal average and $U_J = \langle u_\varphi \rangle_\varphi$ corresponds to the radial profile of the toroidal jets. Since the initial fingers are predominantly radial with $|u_r| \gg |u_\vartheta|$ and the jets are almost concentric with little ϑ dependence (see figure 12), (4.2) can be simplified as follows:

$$\frac{1}{r^2} \frac{\partial}{\partial r} \left(r^2 \overline{\langle u_r u_\varphi \rangle_\varphi} \right) \sim \frac{1}{r^2} \frac{\partial}{\partial r} \left(r^2 \frac{\partial \overline{U_J}}{\partial r} \right). \tag{4.3}$$

To examine this balance in more detail, we compute the volume average of the Reynolds stress tensor via

$$Q_{ij} = \frac{2\pi}{V} \int_{r_i}^{r_o} \left| \int_0^\pi \langle u_i u_j \rangle_\varphi \sin \vartheta \, \mathrm{d}\vartheta \right| r^2 \, \mathrm{d}r, \quad (i,j) \in \{r, \vartheta, \varphi\}^2. \tag{4.4}$$

Figure 18 shows the time evolution of the Reynolds stress tensor for the numerical model already shown in figure 17. Initially, the flow takes the form of elongated fingers with a strong radial coherence, Q_{rr} being two orders of magnitude larger than $Q_{r\vartheta}$ and $Q_{r\varphi}$ and one order of magnitude larger than the horizontal components $Q_{\vartheta\vartheta}$ and $Q_{\varphi\varphi}$. When the secondary instability sets in around $t \approx 4$, horizontal jets develop and $Q_{\varphi\varphi}$ increases exponentially over one viscous diffusion time to finally exceed Q_{rr} beyond $t \approx 5$. The correlation $Q_{r\phi}$ increases concomitantly, while the other Reynolds stress terms remain unchanged. Similarly to the tilting instabilities observed in Rayleigh–Bénard convection (e.g. Goluskin *et al.* 2014), the horizontal shear flow grows from the correlation between the radial and the azimuthal component of the background flow, which here corresponds to the tilt of the fingers. Let us stress here that we observe that the same mechanism is at work for $Pr > 1$ fluids, leading to the formation of multiple alternated jets, in agreement with the Cartesian analysis of Holyer (1984, her figure 1).

Interestingly, close to the lower boundary of the instability domain for jet formation for $Pr < 1$ simulations (figure 16), we found one numerical model (highlighted by a white

988 A18-32
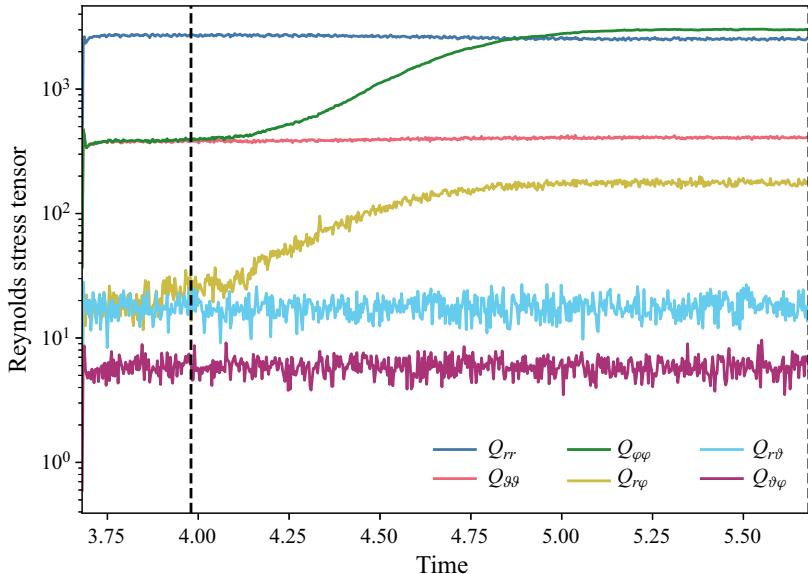
Figure 18. Time evolution of the Reynolds stress tensor Q_{ij} (4.4) for a simulation with $Pr = 0.3$, $Le = 10$, $R_\rho = 5$ and $Ra_\xi = 2 \times 10^8$ (simulation 55 in table 3), and subjected to the enforcement of a twofold azimuthal symmetry, such that the jet that forms has no component along $\boldsymbol{e}_\theta$. The two vertical lines correspond to the snapshots shown in figure 17.

star with a yellow rim) for which the interplay between shear and fingers via Reynolds stresses drives relaxation oscillations. Those are visible in figure 19, which shows the time evolution of the poloidal and toroidal kinetic energy (*a*) alongside that of the Sherwood number (*b*) for a numerical model with $Ra_T = -10^9$, $Pr = 0.3$, $Le = 10$ and $R_\rho = 4$. It comes as no surprise that the temporal evolution of the poloidal energy $E_{k,pol}$ is strongly correlated with that of the chemical transport *Sh*. Relative changes of the two quantities are actually comparable, reaching approximately 5 % of their mean values. This numerical model features a single jet, whose axis of symmetry changes over time. This manifests itself by the relative variations of the axisymmetric toroidal energy, which suddenly grow beyond $t \approx 9$ when the jet comes in better alignment with the *z*-axis. Toroidal and poloidal energies oscillate over time with a typical period close to the viscous diffusion time, a behaviour that resembles that of the 2-D models by Garaud & Brummell (2015). Strong toroidal jets disrupt the fingers, hence reducing the efficiency of the radial flow and heat transport. This in turn is detrimental to feeding the jets via Reynolds stresses. The shear subsequently decays, permitting a more efficient radial transport. Repeating this cycle yields out-of-phase oscillations for $E_{k,pol}$ and $E_{k,tor}$. In agreement with the findings by Xie *et al.* (2019), relaxation oscillations disappear when increasing R_ρ while keeping all the other parameters constant. Conversely, we do not observe jets forming for lower values of R_ρ. This indicates that relaxation oscillations likely mark the boundary of the secondary instability domain.

5. Summary and conclusion

We investigate the properties of fingering convection in a non-rotating spherical shell of radius ratio $r_i/r_o = 0.35$ using a catalogue of 123 three-dimensional simulations, one

(*a*)
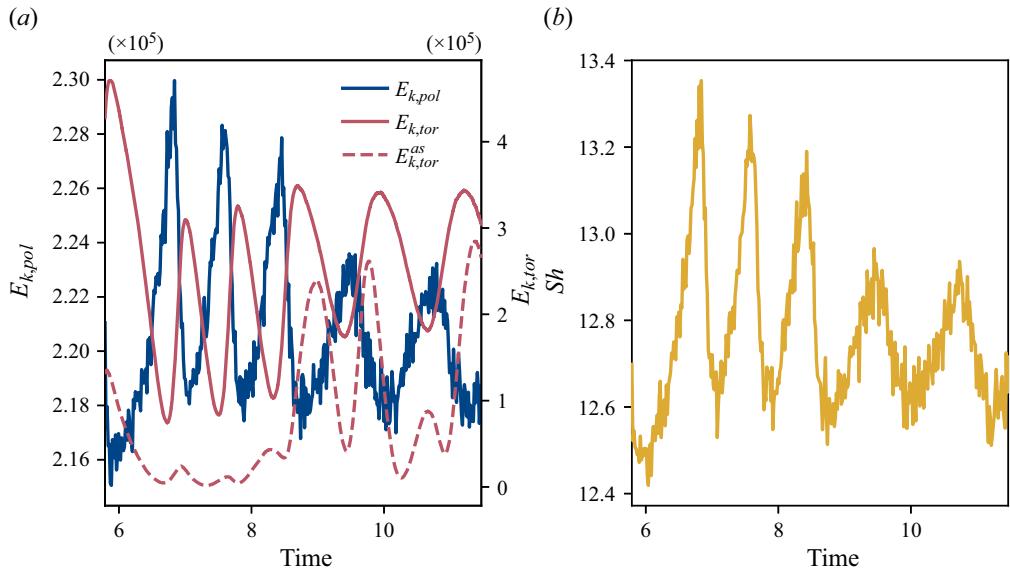
Figure 19. (*a*) Time evolution of the poloidal kinetic energy (solid blue), the toroidal kinetic energy (solid red) and the axisymmetric toroidal energy (dashed red) for a simulation performed with $Ra_T = -10^9$, $Pr = 0.3$, $Le = 10$ and $R_\rho = 4$ (simulation 39 in table 3). (*b*) Time evolution of Sh for that simulation, that is represented with the white star with a yellow rim in figure 16.

of our aims being to examine the extent to which predictions derived in local Cartesian domains would be adequate in a global spherical context. We focus on scaling laws for the transport of composition, heat and momentum, and studied the possible occurrence of jet-forming secondary instabilities, over a broad range of Prandtl numbers, from $Pr = 0.03$ to $Pr = 7$.

In spherical shells, curvature and the linear increase of the gravitational acceleration with radius yield asymmetric boundary layers. A dedicated analysis of the chemical boundary layers enables us to show that (i) the boundary layer asymmetry can be rationalised by assuming that the boundary layers are marginally unstable; (ii) the thickness of the boundary layers is well described by the laminar Prandtl–Blasius model.

A single horizontal scale, defined in practice at mid-depth, suffices to describe the lateral extent of fingers, which does not show substantial variations with radius in the fluid bulk. We show that the typical finger width is controlled by a balance between buoyancy and viscous forces, and that its expression can be derived by making the classical 'tall finger' assumption, whereby along-finger (radial) derivatives are neglected against cross-finger (horizontal) derivatives (see e.g. Taylor & Bucens 1989; Smyth & Kimura 2007). The excellent agreement between the prediction and the dataset seen in figure 7(*b*) stresses the crucial importance of the correction factor involving the flux ratio γ, compared with the original $|Ra_T|^{-1/4}$ scaling proposed by Stern (1960), even though this correction implies the loss of predictivity.

While the law expressing the finger width is adequate for all cases, establishing scaling laws for transport requires us to distinguish between cases close to onset and cases that were strongly driven. To stress the differences and similarities with planar models, table 2

988 A18-34

Quantity	Unbounded Cartesian	Bounded Cartesian	This study
		Weakly nonlinear ($Pr > 1$)	
$\mathcal{L}_h$	$\epsilon^{-1/4}\lvert Ra_T\rvert^{-1/4}$ (R10)	$\epsilon^{-1/4}\lvert Ra_T\rvert^{-1/4}$ (RS00)	$\epsilon^{-1/4}\lvert Ra_T\rvert^{-1/4}$
$Nu - 1$	$\epsilon^2 Le^{-2}$ (R10)	$\epsilon^{13/10}\lvert Ra_T\rvert^{3/10}Le^{-2}$ (RS00)	$\epsilon^{3/2}\lvert Ra_T\rvert^{3/10}Le^{-2}$
$Sh - 1$	ϵ^2 (R10)	$f(R_\rho, Le, Pr)Ra_\xi^{1/3}$ (T67)	$\epsilon^{3/2}\lvert Ra_T\rvert^{3/10}$
$Pe_{\mathcal{L}_h}$	ϵ (R10)	$\epsilon^{3/4}$ (RS00)	$\epsilon\lvert Ra_T\rvert^{3/20}$
Pe	$\epsilon^{5/4}\lvert Ra_T\rvert^{1/4}$ (R10)	$\epsilon\lvert Ra_T\rvert^{1/4}$ (RS00)	$\epsilon\lvert Ra_T\rvert^{2/5}$
γ	R_ρ/Le (R10)	R_ρ/Le (S79)	R_ρ/Le
		Weakly nonlinear ($Pr < 1$)	
$\mathcal{L}_h$	$\epsilon^{-1/4}\lvert Ra_T\rvert^{-1/4}$ (B13)	—	$[(\gamma^{-1} - 1)\lvert Ra_T\rvert]^{-1/4}$
$Nu^\star - 1$	$\epsilon^2 Le^{-2}$ (B13)	—	$\approx (\epsilon^\star Le^{-1}Pr^{1/2})^{1.4}$
$Sh^\star - 1$	ϵ^2 (B13)	—	$\approx (\epsilon^\star Le^{-1}Pr^{1/2})^{1.4}Le^2$
$Pe_{\mathcal{L}_h}$	ϵ (B13)	—	$Pe\mathcal{L}_h$
$Pe\lvert Ra_T\rvert^{-1/4}$	$\epsilon^{5/4}$ (B13)	—	$\approx \epsilon^{\star 0.95}Pr^{0.17}Le^{0.30}$
γ	R_ρ/Le (B13)	—	$R_\rho^\star/Le$
		Strongly driven, $0 < r_\rho \ll 1$	
λ_ξ	Not relevant	$\begin{cases} Pe^{-1/3}\mathcal{L}_h^{2/3} & \text{(Y16)} \\ Pe^{-1/2}\mathcal{L}_h^{1/2} & \text{(HT10)} \end{cases}$	$Pe^{-1/3}\mathcal{L}_h^{2/3}$
$\mathcal{L}_h$	$f(Le, Pr)\lvert Ra_T\rvert^{-1/4}$ (B13)	$\begin{cases} Ra_\xi^{-1/4}R_\rho^{-1/8} & \text{(Y16)} \\ \lvert Ra_T\rvert^{-1/3}Ra_\xi^{1/9} & \text{(HT10)} \end{cases}$	$[(\gamma^{-1} - 1)\lvert Ra_T\rvert]^{-1/4}$
$Sh - 1$	$\begin{cases} f(Pr, Le) & \text{(B13)} \\ (R_\rho - 1)^{-1/2} & \text{(RS12)} \end{cases}$	$\begin{cases} Ra_\xi^{1/3} & \text{(Y16)} \\ f(R_\rho, Le, Pr)Ra_\xi^{1/3} & \text{(T67)} \\ Ra_\xi^{4/9}\lvert Ra_T\rvert^{-1/12} & \text{(HT10)} \end{cases}$	$Ra_\xi^{1/3}$
Pe	$LePr^{1/2}\mathcal{L}_h^{-1}$ (B13)	$\begin{cases} Ra_\xi^{3/4}\lvert Ra_T\rvert^{-1/4}\dfrac{Sc}{Le^{1/4}} & \text{(Y16)} \\ Ra_\xi\lvert Ra_T\rvert^{-1/2}Sc & \text{(HT10)} \end{cases}$	$Ra_\xi^{2/3}\lvert Ra_T\rvert^{-1/4}$
γ	$\begin{cases} R_\rho(1 + LePr)^{1/2} & \text{(B13)} \\ \approx \alpha_1 e^{-\alpha_2 R_\rho} + \alpha_3 & \text{(RS12)} \end{cases}$	$\approx f(Ra_\xi)R_\rho^{-1/4}$ (Y16)	$f(Pr, Le)$?

Table 2. Comparison of the scaling laws reported in unbounded and bounded Cartesian models with the ones obtained in this study. For an easier comparison with existing scaling laws, we define a Péclet number based on the finger width $Pe_{\mathcal{L}_h} = Pe\mathcal{L}_h$. The abbreviation B13 corresponds to Brown *et al.* (2013), HT10 to Hage & Tilgner (2010), RS00 to Radko & Stern (2000), R10 to Radko (2010), RS12 to Radko & Smith (2012), S79 to Schmitt (1979*b*), T67 to Turner (1967) and Y16 to Yang *et al.* (2016). The $\approx$ signs correspond to numerical fits where no theoretical derivation could be provided. The question mark in the last row accounts for an uncertainty on the scaling for γ.

summarises all the scaling laws established in § 3 alongside those reported in unbounded and bounded Cartesian models.

For the weakly nonlinear scalings corresponding to the two first sections of table 2, we introduce a small parameter, $\epsilon = R_\rho/Le - 1$, which measures the distance to onset. We provide novel predictive theoretical scaling laws of the form $\epsilon^{\alpha_1}|Ra_T|^{\alpha_2}Le^{\alpha_3}$ for transport in bounded domains by making use of two cornerstone assumptions: (i) the finger width relates to the width of the fastest growing mode when $\epsilon \ll 1$ (Schmitt 1979*b*); (ii) compositional boundary layers are well described by the Prandtl–Blasius model. Our scaling laws differ – unsurprisingly – from the theoretical derivations carried out in unbounded models but also from the ones derived in bounded models (Radko & Stern 2000). This latter discrepancy originates from the different assumption retained to model the compositional boundary layer. Our simulations with $Pr > 1$ and $\epsilon < 1$ are found to nicely adhere to these new theoretical scalings, while $Pr < 1$ models show less of an agreement. For the latter, several assumptions entering the derivation, such as neglecting the effect of shear and inertia, likely become dubious on decreasing Pr. We nonetheless show that adjusted diagnostics, which incorporate the modification of the background profiles into account for the $Pr < 1$ spherical-shell data, favourably compare with the local unbounded models by Brown *et al.* (2013) and can be described by simple polynomial fits provided in the middle section of table 2. While those numerical fits merely provide a heuristic description of the scaling behaviour of the transport of heat and chemical composition, they have the merit to better describing the $Pr < 1$ data and could prove beneficial for future studies.

For strongly driven cases, corresponding to the last section of table 2, we show that the Sherwood number trends towards the asymptotic dependency of $Ra_\xi^{1/3}$, regardless of the value of Pr, even if a direct numerical verification of this scaling is beyond our computational reach. Our strongly driven cases are not perfectly in the $Ra_\xi \gg 1$ regime, which implies that a non-negligible fraction of dissipation occurs inside the boundary layers. In addition, the mixture of Prandtl numbers within the ensemble of simulations leads to variety of transport mechanisms, and consequently to some residual scatter in figure 11(*a*). The analysis of the power balance in conjunction with $Sh \sim Ra_\xi^{1/3}$ prompts us to propose a novel scaling law for the velocity Pe that accounts extremely well for our data and those of Yang *et al.* (2016). This law is adequate for regimes where fingers dominate the dynamics, regardless of the geometry. Conversely, this law may prove of limited value to account for data obtained for $R_\rho < 1$ (or equivalently $r_\rho < 0$), i.e. when overturning convection can also occur. Among the most salient differences between the scaling behaviours shown in table 2 in this regime, we would like to stress that our simulations with $Pr \ll 1$ feature scaling behaviours for the chemical transport that grow as $Ra_\xi^{1/3}$, in stark contrast with the predictions from unbounded domains which predict a constant value for any given (Pr, Le) pair (Brown *et al.* 2013).

A secondary instability may develop in the form of large-scale toroidal jets. These features have been observed in both unbounded and bounded planar models which – by construction – deal with low aspect ratios, so it was far from clear that they could actually grow in a global geometry. Here, we report for the first time on large-scale toroidal jets that develop in non-rotating spherical shells. If the properties and evolution of those jets depend on the Prandtl number being larger or smaller than unity, their formation is in any event contingent upon a minimum level of driving. For low Pr fluids, a single jet develops and we find that the level of forcing leading to jet formation

is bounded, meaning that jets might disappear in the $Ra_\xi \gg 1$ limit, all other control parameters remaining fixed. In addition, our results indicate that the interval of forcing over which jet formation occurs shrinks as Pr decreases. Consequently, we do not expect toroidal jets to form in spherical geometry in the $Pr \ll 1$ limit, in agreement with the conclusion drawn by Garaud & Brummell (2015) in Cartesian geometry. For Pr above unity, multiple alternated jets form, and our numerical results suggest that there is no upper bound on the level of forcing that favours jet formation. We were not able to study the possible merging of those multiple jets in a systematic manner, due to the computational cost of such an investigation, as the merging and subsequent saturation may occur on a time scale commensurate with the viscous time scale. The analysis and characterisation of the merging process appear as pending issues worthy of future examination. As envisioned by Holyer (1984) and Stern & Simeonov (2005), jets draw their energy from the Reynolds stress correlations that come from the sheared fingers, a mechanism akin to the tilting instabilities found in classical Rayleigh–Bénard convection (e.g. Goluskin *et al.* 2014). The nonlinear saturation of this secondary instability can yield relaxation oscillations with a quasi-periodic exchange of energy between fingers and jets. We finally note that a more detailed description of the region of parameter space where jets may develop would entail a linearisation to be performed around the fingering convection state, a task which is not straightforward in a global spherical geometry.

Fingering convection can eventually lead to the formation of compositional staircases. Staircases were found by Stellmach *et al.* (2011) in a triply periodic domain, and more recently by Yang (2020) in a bounded Cartesian configuration, upon reaching $Ra_\xi \gtrsim 10^{12}$, slightly above the maximum value considered in this work ($Ra_\xi = 5 \times 10^{11}$). Future work should seek confirmation of spontaneous layer formation in a spherical shell.

Finally, let us recall that this study ignored the effect of background rotation from the outset, on account of parsimony. In view of planetary applications, and in light of the studies by Monville *et al.* (2019) and Guervilly (2022), a sensible next step is to add background rotation to the physical set-up and to analyse how it affects the understanding developed here in the non-rotating case.

Author ORCIDs.

ⓘ Thomas Gastine https://orcid.org/0000-0003-4438-7203;

ⓘ Alexandre Fournier https://orcid.org/0000-0003-3276-0496.

Appendix A. Numerical database

#	$|Ra_T|$ $(\times 10^7)$	(N_r, ℓ_{max})	R_ρ	$R_\rho^\star$	γ	$E_{k,tor}^\%$	Nu	Sh	(λ_i, λ_o) $(\times 10^{-1})$	$(\Delta_{i,\Xi}, \Delta_{o,\Xi})$	Re_{pol}	Re_{tor}^1	ℓ_h
						$Pr = 0.03, Le = 33.3$							
1	6.6	(513, 426)	1.10	2.86	0.42	22.00	1.33	31.31	(0.06, 0.07)	(0.43, 0.06)	1201.4	17.3	74
2	6.6	(241, 213)	8.25	13.26	0.61	12.48	1.02	10.23	(0.12, 0.14)	(0.29, 0.04)	290.3	5.0	61
3	6.6	(217, 213)	15.40	19.98	0.71	8.96	1.01	4.90	(0.18, 0.21)	(0.20, 0.03)	140.4	3.2	54
4	6.6	(193, 213)	22.44	25.32	0.81	5.84	1.00	2.39	(0.30, 0.33)	(0.16, 0.02)	67.3	2.1	47
5	6.6	(193, 213)	23.00	25.76	0.81	5.60	1.00	2.26	(0.32, 0.35)	(0.16, 0.02)	62.9	2.4	46
6	6.6	(193, 213)	27.50	29.04	0.88	4.89	1.00	1.47	(0.00, 0.00)	(0.00, 0.00)	32.6	4.6	40
7	6.6	(193, 213)	28.00	29.42	0.89	4.38	1.00	1.41	(0.00, 0.00)	(0.00, 0.00)	29.7	3.9	39
8	0.66	(201, 213)	1.10	3.95	0.43	20.23	1.19	18.03	(0.12, 0.14)	(0.50, 0.07)	528.9	13.6	40
9	0.66	(129, 128)	2.95	8.23	0.51	15.57	1.06	12.13	(0.16, 0.19)	(0.46, 0.07)	285.5	7.7	37
10	0.66	(129, 128)	8.25	15.78	0.64	11.00	1.01	6.59	(0.25, 0.28)	(0.37, 0.05)	128.5	4.3	32
11	0.66	(129, 128)	15.40	21.76	0.73	7.74	1.00	3.46	(0.37, 0.40)	(0.29, 0.04)	63.0	2.5	28
12	0.66	(129, 128)	22.44	26.39	0.82	4.89	1.00	1.91	(0.72, 0.66)	(0.27, 0.04)	30.8	1.4	24
13	0.066	(97, 133)	1.10	5.99	0.43	17.53	1.09	9.86	(0.25, 0.29)	(0.56, 0.08)	223.0	10.2	22
						$Pr = 0.1, Le = 30$							
14	73.34	(385, 426)	6.80	10.86	0.61	7.43	1.06	21.67	(0.05, 0.07)	(0.28, 0.04)	285.8	2.9	118
15	7.334	(321, 213)	1.10	3.49	0.48	13.29	1.52	37.90	(0.05, 0.06)	(0.47, 0.07)	493.3	6.2	73
16	7.334	(241, 213)	6.80	13.01	0.63	6.35	1.04	14.02	(0.11, 0.13)	(0.36, 0.05)	127.6	2.9	64
17	7.334	(217, 213)	8.00	14.31	0.65	5.79	1.03	12.19	(0.12, 0.14)	(0.33, 0.05)	109.3	2.2	63
18	7.334	(217, 213)	10.00	16.23	0.68	5.07	1.02	9.76	(0.13, 0.16)	(0.30, 0.05)	86.3	3.0	60
19*	7.334	(241, 213)	11.00	16.77	0.69	38.62	1.02	8.45	(0.14, 0.17)	(0.28, 0.04)	76.4	58.0	59
20*	7.334	(241, 213)	12.60	18.20	0.71	40.09	1.01	7.05	(0.15, 0.18)	(0.25, 0.04)	64.2	50.9	57
21*	7.334	(217, 213)	14.00	19.38	0.73	36.43	1.01	6.07	(0.16, 0.19)	(0.23, 0.04)	55.4	40.4	56
22*	7.334	(217, 213)	15.00	20.16	0.75	32.40	1.01	5.47	(0.17, 0.20)	(0.22, 0.03)	49.9	33.1	55
23*	7.334	(217, 213)	16.00	20.91	0.76	27.57	1.01	4.93	(0.18, 0.21)	(0.21, 0.03)	44.9	27.1	54
24*	7.334	(217, 213)	17.00	21.67	0.78	22.28	1.01	4.44	(0.19, 0.23)	(0.20, 0.03)	40.4	20.9	53
25*	7.334	(217, 213)	18.40	22.69	0.80	13.88	1.00	3.85	(0.21, 0.24)	(0.18, 0.03)	34.7	13.4	51
26	0.7334	(129, 128)	1.10	5.27	0.49	10.99	1.27	20.43	(0.12, 0.12)	(0.55, 0.07)	206.5	4.6	40
27	0.7334	(129, 128)	6.80	15.74	0.66	5.13	1.02	8.46	(0.22, 0.26)	(0.43, 0.07)	54.2	1.7	33
28	0.7334	(129, 128)	12.60	20.56	0.75	3.19	1.01	4.80	(0.31, 0.35)	(0.34, 0.05)	28.0	1.1	30
29	0.7334	(129, 128)	18.40	24.17	0.83	1.71	1.00	2.82	(0.44, 0.46)	(0.27, 0.04)	15.1	0.6	26
30	0.7334	(129, 128)	24.20	27.07	0.90	0.40	1.00	1.57	(0.00, 0.00)	(0.00, 0.00)	6.6	0.2	22

Table 3. For caption see on next page.

#	$\|Ra_T\|$ $(\times 10^7)$	(N_r, ℓ_{max})	R_ρ	$R_\rho^\star$	γ	$E_{k,tor}^\%$	Nu	Sh	(λ_i, λ_o) $(\times 10^{-1})$	$(\Delta_i \Xi, \Delta_o \Xi)$	Re_{pol}	Re_{tor}^1	ℓ_h
31	0.0733	(49, 85)	1.10	7.81	0.48	8.35	1.13	10.73	(0.25, 0.27)	(0.60, 0.09)	83.4	3.2	22
32	0.0073	(41, 85)	1.10	10.66	0.44	6.26	1.06	5.64	(0.52, 0.55)	(0.64, 0.09)	33.1	2.0	12
						$Pr = 0.3, Le = 10$							
33*	1000	(433, 682)	5.00	5.75	0.72	80.96	1.14	10.86	(0.04, 0.05)	(0.11, 0.02)	253.6	510.2	200
34*	1000	(321, 597)	7.30	7.69	0.82	79.67	1.03	3.70	(0.07, 0.08)	(0.06, 0.01)	103.7	204.1	174
35*	1000	(321, 597)	9.30	9.42	0.95	1.98	1.01	1.51	(0.00, 0.00)	(0.00, 0.00)	30.2	3.9	134
36	202	(541, 682)	1.01	1.99	0.60	12.23	4.12	53.74	(0.03, 0.03)	(0.38, 0.05)	879.5	5.9	139
37	150	(433, 512)	1.50	2.74	0.62	9.34	2.54	38.55	(0.04, 0.04)	(0.35, 0.05)	563.1	3.8	134
38	100	(289, 341)	3.50	5.03	0.69	5.51	1.30	16.10	(0.06, 0.07)	(0.23, 0.03)	210.1	6.0	119
39*	100	(241, 341)	4.00	5.36	0.70	52.90	1.21	12.77	(0.07, 0.08)	(0.20, 0.03)	173.9	187.0	115
40*	100	(241, 341)	5.00	6.08	0.74	77.61	1.11	8.18	(0.08, 0.10)	(0.16, 0.02)	121.4	229.9	109
41*	100	(193, 341)	6.00	6.87	0.77	72.19	1.06	5.50	(0.10, 0.12)	(0.12, 0.02)	86.3	138.1	103
42*	100	(193, 341)	7.00	7.69	0.82	54.91	1.03	3.70	(0.12, 0.14)	(0.10, 0.02)	59.7	65.2	97
43*	100	(193, 341)	8.00	8.50	0.87	7.20	1.02	2.64	(0.15, 0.18)	(0.09, 0.01)	40.2	11.2	90
44	100	(193, 341)	9.00	9.36	0.93	1.10	1.01	1.66	(0.00, 0.00)	(0.00, 0.00)	20.5	1.5	76
45	30	(257, 341)	1.50	3.15	0.62	8.31	2.08	27.39	(0.06, 0.07)	(0.40, 0.06)	316.9	3.2	90
46	22	(257, 341)	1.10	2.61	0.61	9.69	2.62	30.83	(0.06, 0.07)	(0.44, 0.06)	366.4	4.1	82
47	20.2	(289, 341)	1.01	2.48	0.60	10.12	2.80	31.70	(0.06, 0.07)	(0.45, 0.06)	380.6	4.3	79
48	18	(129, 170)	9.00	9.49	0.94	0.42	1.01	1.48	(0.00, 0.00)	(0.00, 0.00)	11.1	0.3	46
49	10	(193, 213)	1.50	3.51	0.63	7.44	1.84	21.43	(0.09, 0.09)	(0.43, 0.06)	211.7	2.9	68
50	10	(161, 213)	3.00	5.27	0.69	5.31	1.26	12.51	(0.11, 0.14)	(0.33, 0.05)	111.2	5.0	65
51*	10	(129, 170)	3.25	5.40	0.70	54.68	1.21	11.00	(0.12, 0.14)	(0.31, 0.05)	100.2	96.4	64
52*	10	(129, 170)	3.50	5.62	0.71	56.27	1.18	10.07	(0.12, 0.15)	(0.30, 0.04)	91.9	89.3	63
53*	10	(129, 170)	4.00	5.99	0.72	55.80	1.13	8.47	(0.14, 0.16)	(0.27, 0.04)	77.9	81.5	62
54*	10	(129, 170)	4.50	6.43	0.74	52.16	1.10	7.16	(0.15, 0.17)	(0.25, 0.04)	66.4	57.1	60
55*	10	(129, 170)	5.00	6.78	0.76	45.30	1.08	6.10	(0.16, 0.19)	(0.22, 0.03)	56.8	50.8	59
56*	10	(129, 170)	5.50	7.17	0.78	36.75	1.06	5.18	(0.17, 0.20)	(0.21, 0.03)	48.5	31.5	57
57*	10	(129, 170)	6.00	7.50	0.80	25.17	1.05	4.42	(0.18, 0.22)	(0.19, 0.03)	41.3	21.8	56
58	10	(129, 170)	7.00	8.20	0.85	5.04	1.03	3.21	(0.22, 0.26)	(0.16, 0.02)	29.1	5.3	52
59	10	(129, 170)	8.00	8.91	0.89	1.41	1.01	2.22	(0.32, 0.33)	(0.15, 0.02)	18.6	1.1	46
60	10	(129, 170)	9.00	9.47	0.94	0.32	1.00	1.42	(0.00, 0.00)	(0.00, 0.00)	8.9	0.2	39

Table 3. For caption see on next page.

#	$|Ra_T|$ $(\times 10^7)$	(N_r, ℓ_{max})	R_ρ	$R_\rho^\star$	γ	$E^\%_{k,tor}$	Nu	Sh	(λ_i, λ_o) $(\times 10^{-1})$	$(\Delta_i\varXi, \Delta_o\varXi)$	Re_{pol}	Re^1_{tor}	ℓ_h
61	3	(129, 170)	1.50	3.96	0.64	6.70	1.62	16.08	(0.12, 0.14)	(0.47, 0.07)	134.7	3.7	47
62	2.2	(129, 170)	1.10	3.37	0.61	7.69	1.89	17.54	(0.12, 0.14)	(0.50, 0.07)	153.7	3.1	46
63	2.06	(129, 170)	1.03	3.26	0.61	7.91	1.95	17.81	(0.12, 0.14)	(0.51, 0.07)	157.9	3.0	45
64	2.02	(129, 170)	1.01	3.22	0.61	7.99	1.98	17.89	(0.12, 0.14)	(0.51, 0.07)	159.1	3.1	45
65	1	(65, 128)	5.00	7.47	0.79	2.68	1.05	4.26	(0.32, 0.36)	(0.31, 0.05)	24.7	1.0	30
66	0.3	(65, 128)	1.50	5.00	0.65	5.20	1.33	9.03	(0.25, 0.30)	(0.52, 0.08)	55.0	1.8	26
67	0.03	(65, 128)	1.50	5.39	0.64	3.95	1.16	4.97	(0.53, 0.58)	(0.57, 0.09)	22.0	1.1	14
68	0.01	(65, 85)	5.00	7.86	0.81	0.58	1.01	1.81	(1.73, 1.51)	(0.56, 0.09)	4.0	0.2	8
							$Pr = 1, Le = 10$						
69	300	(601, 794)	1.50	3.22	0.63	3.63	3.33	57.20	(0.03, 0.03)	(0.41, 0.06)	255.8	1.6	165
70	150	(433, 629)	1.50	3.44	0.63	3.36	3.00	48.94	(0.04, 0.04)	(0.43, 0.06)	198.5	2.0	139
71	15	(257, 341)	1.10	3.57	0.63	3.19	2.76	32.79	(0.07, 0.08)	(0.51, 0.07)	107.4	2.1	77
72*	15	(257, 341)	1.30	3.85	0.63	25.26	2.35	29.63	(0.07, 0.08)	(0.49, 0.07)	93.1	51.8	77
73*	15	(257, 341)	1.50	4.23	0.64	30.21	2.10	27.42	(0.07, 0.09)	(0.48, 0.07)	82.5	58.6	77
74	15	(257, 341)	2.00	5.26	0.68	3.94	1.77	24.00	(0.08, 0.10)	(0.46, 0.07)	64.5	8.6	77
75	15	(257, 341)	5.00	8.12	0.83	0.80	1.15	10.34	(0.12, 0.15)	(0.29, 0.05)	23.0	0.8	63
76	15	(257, 341)	7.00	8.97	0.89	0.25	1.05	4.99	(0.17, 0.19)	(0.19, 0.03)	11.5	0.2	54
77	15	(257, 341)	8.00	9.27	0.92	0.09	1.02	3.00	(0.22, 0.23)	(0.15, 0.02)	7.2	0.1	49
78	15	(257, 341)	9.00	9.59	0.95	0.02	1.01	1.58	(0.00, 0.00)	(0.00, 0.00)	4.1	0.0	30
79	1.5	(121, 170)	1.50	6.09	0.70	1.57	1.65	15.74	(0.15, 0.19)	(0.54, 0.09)	32.8	0.8	41
							$Pr = 3, Le = 10$						
80*NS	750	(769, 938)	1.50	3.58	0.62	10.62	4.48	85.48	(0.02, 0.02)	(0.44, 0.06)	134.3	39.2	218
81*NS	300	(541, 682)	1.50	3.98	0.63	15.19	3.85	69.49	(0.03, 0.03)	(0.47, 0.06)	94.9	39.5	174
82*	150	(541, 682)	1.05	3.25	0.61	48.63	4.84	68.32	(0.03, 0.03)	(0.51, 0.07)	99.2	95.6	139
83*	150	(541, 682)	1.20	3.57	0.61	51.80	4.15	63.64	(0.03, 0.04)	(0.49, 0.07)	87.7	90.2	142
84*	150	(433, 597)	1.50	4.40	0.64	3.65	3.46	58.92	(0.04, 0.04)	(0.49, 0.07)	72.6	9.6	145
85*	150	(481, 629)	2.00	5.13	0.67	7.55	2.59	49.04	(0.04, 0.05)	(0.45, 0.07)	56.0	15.4	145
86	150	(481, 629)	3.00	7.44	0.79	0.44	2.03	40.38	(0.04, 0.06)	(0.43, 0.07)	37.6	1.3	127
87	150	(481, 629)	5.00	8.64	0.86	0.21	1.37	22.71	(0.06, 0.08)	(0.31, 0.05)	19.7	0.5	112
88	150	(481, 512)	7.00	9.12	0.91	0.03	1.12	10.18	(0.07, 0.09)	(0.18, 0.03)	9.9	0.1	97
89	150	(385, 629)	8.00	9.32	0.93	0.01	1.05	5.48	(0.09, 0.11)	(0.12, 0.02)	6.2	0.0	90
90	150	(481, 629)	9.00	9.56	0.95	0.00	1.01	2.26	(0.17, 0.16)	(0.08, 0.01)	2.9	0.0	81

Table 3. For caption see on next page.

#	$|Ra_T|$ ($\times 10^7$)	(N_r, ℓ_{max})	R_ρ	$R_\rho^\star$	γ	$E^\%_{k,tor}$	Nu	Sh	(λ_i, λ_o) ($\times 10^{-1}$)	$(\Delta_i \Xi, \Delta_o \Xi)$	Re_{pol}	Re^1_{tor}	ℓ_h
91	15	(193, 320)	5.00	8.56	0.86	0.04	1.18	11.71	(0.12, 0.15)	(0.32, 0.05)	7.7	0.1	59
92	15	(193, 320)	6.00	8.77	0.88	0.02	1.10	8.18	(0.14, 0.17)	(0.26, 0.04)	5.6	0.0	56
93	15	(193, 320)	7.00	8.99	0.90	0.01	1.06	5.34	(0.17, 0.19)	(0.20, 0.03)	3.9	0.0	53
94	15	(193, 320)	8.00	9.24	0.93	0.01	1.02	3.13	(0.22, 0.23)	(0.16, 0.02)	2.4	0.0	49
95	15	(193, 320)	9.00	9.53	0.95	0.00	1.01	1.60	(0.00, 0.00)	(0.00, 0.00)	1.1	0.0	43
96	1.5	(97, 170)	7.00	8.94	0.90	0.01	1.03	3.03	(0.39, 0.40)	(0.26, 0.04)	1.5	0.0	28
97	1.5	(97, 170)	8.00	9.22	0.92	0.00	1.01	1.98	(0.63, 0.54)	(0.25, 0.03)	1.0	0.0	26
98	1.5	(97, 170)	9.00	9.51	0.95	0.00	1.00	1.27	(0.00, 0.00)	(0.00, 0.00)	0.4	0.0	23
99	0.15	(73, 106)	1.50	7.11	0.74	0.06	1.34	8.40	(0.32, 0.39)	(0.60, 0.10)	4.2	0.0	21
							$Pr = 7, Le = 3$						
100*NS	18300	(1536, 1536)	1.10	1.56	0.78	13.58	25.03	102.9	(0.01, 0.01)	(0.30, 0.04)	312.4	119.4	339
101*NS	1830	(641, 970)	1.10	1.74	0.77	18.29	14.50	58.78	(0.02, 0.03)	(0.35, 0.05)	128.6	58.6	205
102	833.3	(385, 469)	2.50	2.87	0.95	0.09	1.89	7.95	(0.06, 0.08)	(0.11, 0.02)	15.5	0.3	131
103*NS	732	(481, 629)	1.10	1.80	0.77	18.19	11.78	47.10	(0.03, 0.04)	(0.37, 0.05)	90.6	38.9	166
104	667	(385, 469)	2.00	2.65	0.90	0.33	3.70	19.02	(0.05, 0.06)	(0.22, 0.03)	30.7	1.1	149
105*	500	(385, 426)	1.50	2.20	0.81	11.48	5.84	27.61	(0.04, 0.05)	(0.29, 0.04)	47.8	16.6	159
106*	366	(385, 469)	1.001	1.75	0.77	40.59	11.82	43.66	(0.04, 0.04)	(0.40, 0.05)	80.0	65.5	133
107*	366	(385, 469)	1.05	1.81	0.77	41.38	10.81	41.40	(0.04, 0.04)	(0.39, 0.05)	73.9	61.5	137
108*	366	(385, 426)	1.10	1.88	0.78	17.83	10.18	40.11	(0.04, 0.04)	(0.39, 0.05)	68.9	32.0	142
109*	366	(385, 469)	1.25	2.03	0.79	14.36	7.92	33.96	(0.04, 0.05)	(0.35, 0.05)	56.5	22.7	146
110*	366	(385, 469)	1.50	2.24	0.82	8.45	5.55	25.95	(0.05, 0.06)	(0.30, 0.04)	42.4	12.6	146
111	366	(385, 469)	1.75	2.51	0.87	0.54	4.44	21.85	(0.05, 0.07)	(0.27, 0.04)	32.4	1.9	135
112	366	(385, 469)	2.00	2.72	0.91	0.29	3.40	16.67	(0.06, 0.08)	(0.23, 0.04)	24.3	0.8	124
113	366	(385, 469)	2.50	2.86	0.95	0.04	1.71	6.39	(0.08, 0.10)	(0.12, 0.02)	11.0	0.1	103
114	366	(385, 469)	2.75	2.91	0.96	0.01	1.19	2.65	(0.12, 0.13)	(0.08, 0.01)	5.3	0.0	94
115	366	(385, 469)	2.90	2.95	0.98	0.00	1.03	1.29	(0.00, 0.00)	(0.00, 0.00)	1.9	0.0	80
116	366	(385, 469)	2.95	2.97	0.99	0.00	1.01	1.07	(0.00, 0.00)	(0.00, 0.00)	0.9	0.0	70
117*	350	(385, 469)	1.05	1.81	0.77	39.71	10.70	40.97	(0.04, 0.04)	(0.39, 0.05)	72.6	58.3	136
118	36.6	(193, 256)	1.10	2.29	0.82	0.50	6.50	23.48	(0.08, 0.10)	(0.45, 0.07)	27.7	1.2	75
119	36.6	(193, 256)	2.70	2.89	0.96	0.01	1.13	2.13	(0.27, 0.27)	(0.13, 0.02)	2.6	0.0	50
120	36.6	(193, 256)	2.79	2.91	0.97	0.00	1.06	1.56	(0.00, 0.00)	(0.00, 0.00)	1.7	0.0	48

Table 3. For caption see on next page.

#	$|Ra_T|$ ($\times 10^7$)	(N_r, ℓ_{max})	R_ρ	$R_\rho^\star$	γ	$E_{k,tor}^\%$	Nu	Sh	(λ_i, λ_o) ($\times 10^{-1}$)	$(\Delta_i\Xi, \Delta_o\Xi)$	Re_{pol}	Re_{tor}^1	ℓ_h
121	36.6	(193, 256)	2.89	2.95	0.98	0.00	1.02	1.16	(0.00, 0.00)	(0.00, 0.00)	0.8	0.0	43
122	36.6	(193, 256)	2.94	2.97	0.99	0.00	1.00	1.04	(0.00, 0.00)	(0.00, 0.00)	0.4	0.0	39
123	3.66	(129, 170)	1.10	2.55	0.85	0.11	3.84	12.37	(0.17, 0.23)	(0.49, 0.08)	10.3	0.1	39

Table 3. Control parameters and output diagnostics for the 123 simulations performed for this study. Simulations are sorted according to increasing Pr, then increasing Ra_T and finally increasing R_ρ. The quantity $E_{k,tor}^\%$ is the fraction of kinetic energy contained in the toroidal flow, expressed in per cent. The single simulation resorting to finite differences in the radial direction is indicated with the f superscript next to the value of N_r. A star in the leftmost column indicates simulations featuring jets, with an additional 'NS' if the jets had yet to reach saturation.

Appendix B. Heat sources in spherical geometry

This appendix demonstrates how the time-averaged buoyancy powers $\mathcal{P}_\xi$ and $\mathcal{P}_T$ can be related to $Ra_\xi(Sh-1)/Sc^2$ and $Ra_T(Nu-1)/Pr^2$ in spherical geometry. In contrast to the planar configuration, where those quantities match each other, gravity changes with radius and curvature prohibit such an exact relation in curvilinear geometries (see the derivations by Oruba 2016). Here, we detail the main steps involved in the approximation of $\mathcal{P}_\xi$ only, keeping in mind that the derivation $\mathcal{P}_T$ would be strictly the same with simple exchanges of Ra_ξ by Ra_T, Sh by Nu and Sc by Pr.

To provide an approximation of the time-averaged buoyancy power of chemical origin $\mathcal{P}_\xi$, we first start by noting that

$$\mathcal{P}_\xi = \frac{Ra_\xi}{Sc} \overline{\langle g u_r \xi \rangle_V} = \frac{3 Ra_\xi}{Sc(r_o^3 - r_i^3)} \int_{r_i}^{r_o} g \overline{\langle u_r \xi \rangle_S}\, r^2\, \mathrm{d}r. \tag{B1}$$

Using the definition of the Sherwood number at all radii given in (2.15a,b), we obtain

$$\mathcal{P}_\xi = \frac{3 Ra_\xi}{Sc(r_o^3 - r_i^3)} \left[-\frac{Sh}{Sc} \int_{r_i}^{r_o} g \frac{\mathrm{d}\xi_c}{\mathrm{d}r} r^2\, \mathrm{d}r + \frac{1}{Sc} \int_{r_i}^{r_o} g \frac{\mathrm{d}\varXi}{\mathrm{d}r} r^2\, \mathrm{d}r \right]. \tag{B2}$$

At this stage, it is already quite clear that only the peculiar configuration of $g \propto r^{-2}$ would allow a closed form for the buoyancy power (see Gastine *et al.* 2015). Noting that the conducting background state reads $\mathrm{d}\xi_c/\mathrm{d}r = -r_i r_o/r^2$ and that here $g = r/r_o$, one gets

$$\mathcal{P}_\xi = \frac{3 Ra_\xi}{Sc(r_o^3 - r_i^3)} \left[\frac{1}{2}(r_o^2 - r_i^2) r_i \frac{Sh}{Sc} + \frac{1}{Sc} \int_{r_i}^{r_o} g \frac{\mathrm{d}\varXi}{\mathrm{d}r} r^2\, \mathrm{d}r \right]. \tag{B3}$$

Splitting the time-averaged radial profile of composition into the mean conducting state and a fluctuation such that $\varXi = \xi_c + \varXi'$ yields

$$\mathcal{P}_\xi = \frac{Ra_\xi}{Sc^2} \left[\frac{3}{2} \frac{r_i(r_o + r_i)}{r_o^2 + r_o r_i + r_i^2}(Sh-1) + \frac{3}{r_o(r_o^3 - r_i^3)(Sh-1)} \int_{r_i}^{r_o} \frac{\mathrm{d}\varXi'}{\mathrm{d}r} r^3\, \mathrm{d}r \right]. \tag{B4}$$

The chemical composition being imposed at both boundaries $\varXi'(r_i) = \varXi'(r_o) = 0$, an integration by part of the above expression yields

$$\mathcal{P}_\xi = \frac{Ra_\xi}{Sc^2} \left[\frac{3}{2} \frac{r_i(r_o + r_i)}{r_o^2 + r_o r_i + r_i^2}(Sh-1) - \frac{3}{r_o(Sh-1)} \langle \varXi' \rangle_V \right]. \tag{B5}$$

The second term in the brackets is proportional to the volume- and time-averaged fluctuations of chemical composition. With the choice of imposed composition at both spherical-shell boundaries, this quantity remains bounded within $-1 \leq \langle \varXi' \rangle_V \leq 1$. This second term is hence expected to play a negligible role when $Sh \gg 1$. A fair approximation of $\mathcal{P}_\xi$ in the spherical shell when $g = r/r_o$ thus reads

$$\mathcal{P}_\xi \approx \frac{3}{2} \frac{r_i(r_o + r_i)}{r_o^2 + r_o r_i + r_i^2} \frac{Ra_\xi}{Sc^2}(Sh-1) \approx \frac{4\pi}{V} r_i r_m \frac{Ra_\xi}{Sc^2}(Sh-1), \tag{B6}$$

where V is the spherical-shell volume and $r_m = (r_i + r_o)/2$ is the mid-shell radius. This approximation was already derived by Christensen & Aubert (2006) in the case of thermal convection.
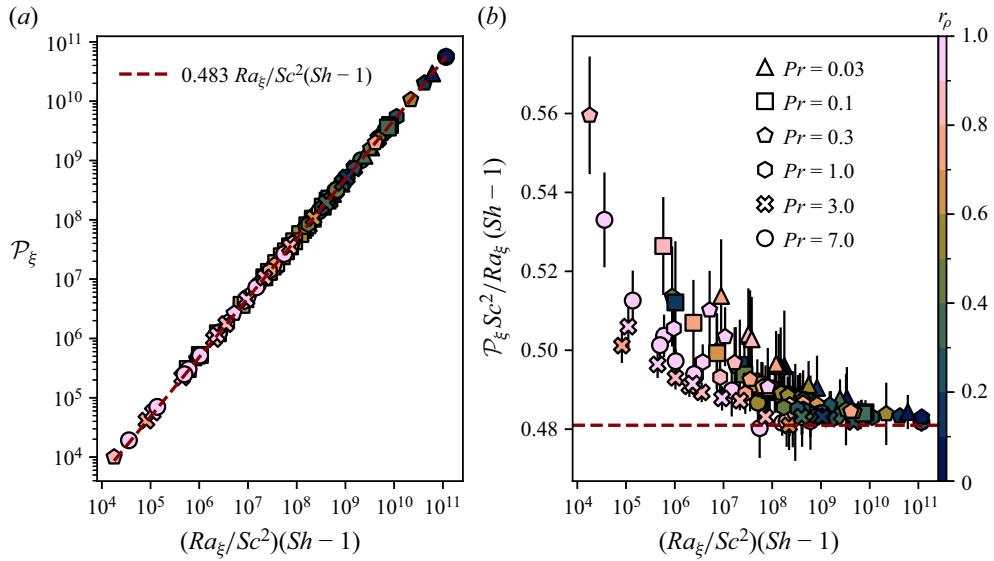
Figure 20. (*a*) Value of $\mathcal{P}_\xi$ as a function of $Ra_\xi Sc^{-2}(Sh - 1)$. The dashed line corresponds to a linear fit to the data. (*b*) Compensated scaling of $\mathcal{P}_\xi Ra_\xi^{-1} Sc^2 (Sh - 1)^{-1}$ as a function of $Ra_\xi Sc^{-2}(Sh - 1)$. The horizontal line corresponds to the theoretical value derived in (B6) for spherical shells with $r_i/r_o = 0.35$.

Figure 20(*a*) shows $\mathcal{P}_\xi$ as a function of $Ra_\xi Sc^{-2}(Sh - 1)$ for the simulations computed in this study. A numerical fit to the data yields

$$\mathcal{P}_\xi = 0.483 \frac{Ra_\xi}{Sc^2}(Sh - 1), \tag{B7}$$

in excellent agreement with the approximated prefactor of 0.481 obtained in (B6) for spherical shells with $r_i/r_o = 0.35$. To highlight the deviations to this approximated scaling, figure 20(*b*) shows the compensated scaling of $\mathcal{P}_\xi Ra_\xi^{-1} Sc^2 (Sh - 1)^{-1}$ as a function of $Ra_\xi Sc^{-2}(Sh - 1)$. As expected, the time-averaged buoyancy power gradually tends towards the scaling (B6) for increasing values of $Ra_\xi (Sh - 1)$.

Appendix C. A comparison with local unbounded simulations for $Pr < 1$

To compare our computations with local Cartesian unbounded models, we introduce adjusted diagnostics which take the modification of the background profiles into account. This practically defines effective quantities on the fluid bulk only

$$\epsilon^\star = \frac{Le}{R_\rho^\star} - 1, \quad Nu^\star - 1 = \frac{Nu - 1}{\mathrm{d}\Theta/\mathrm{d}r(r_m)}, \quad Sh^\star - 1 = \frac{Sh - 1}{|\mathrm{d}\Xi/\mathrm{d}r(r_m)|}, \tag{C1a–c}$$

where the background radial gradients of Θ and Ξ are evaluated at the mid-shell radius. The introduction of these bulk gradients prevents the derivation of scaling laws that solely depend on control quantities, but this is the price to pay to make a comparison with local unbounded models possible. Assuming boldly that the convective and compositional heat transport $Nu^\star - 1$ and $Sh^\star - 1$ can be described by polynomial scaling laws of the form $\epsilon^{\star\alpha_1} Pr^{\alpha_2} Le^{\alpha_3}$ and conducting a 3-parameter least-squares fit on the exponents α_1, α_2 and

988 A18-44
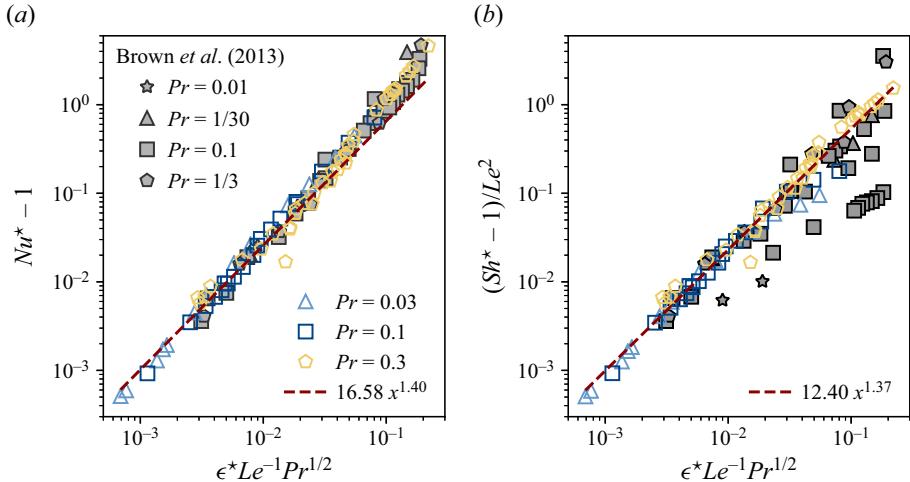
Figure 21. (*a*) Convective heat transport $Nu^\star - 1$ as a function of $\epsilon^\star Le^{-1}Pr^{1/2}$ for our simulations with $Pr < 1$ alongside the unbounded Cartesian simulations from Brown *et al.* (2013). (*b*) Convective transport of chemical composition $(Sh^\star - 1)/Le^2$ as a function of $\epsilon^\star Le^{-1}Pr^{1/2}$. The dashed lines correspond to best fits for the simulations with $\epsilon^\star/Le < 0.05$. Data from Brown *et al.* (2013) come from their table 1.

α_3 for all the simulations with $Pr < 1$ and $\epsilon^\star/Le < 0.05$ yields

$$Nu^\star - 1 \sim \epsilon^{\star 1.43} Pr^{0.68} Le^{-1.40}, \quad (Sh^\star - 1)/Le^2 \sim \epsilon^{\star 1.33} Pr^{0.69} Le^{-1.39}. \qquad \text{(C2a,b)}$$

These numerical fits are suggestive of a simpler parameter dependence of the form

$$Nu^\star - 1 \sim (Sh^\star - 1)/Le^2 \sim \left(\epsilon^\star Le^{-1} Pr^{1/2} \right)^{\alpha_1}. \qquad \text{(C3)}$$

To illustrate this parameter dependence, figure 21 shows $Nu^\star - 1$ and $(Sh^\star - 1)/Le^2$ as a function of $\epsilon^\star Le^{-1}Pr^{1/2}$ for all our 68 numerical simulations with $Pr < 1$ (coloured symbols) alongside 43 local computations from Brown *et al.* (2013) (grey symbols). It is striking to note that our spherical-shell data almost perfectly collapse with the local Cartesian unbounded computations. Weakly nonlinear models with the smallest $\epsilon^\star$ values are compatible with the simple power law (C3) with a scaling exponent $\alpha_1 \approx 1.40$, while a gradual steepening of the slope is observed on increasing supercriticalities. The scaling behaviour of $(Sh^\star - 1)/Le^2$ also shows more scatter when $\epsilon^\star Le^{-1}Pr^{1/2} > 10^{-2}$. This likely comes from the approximation of the flux ratio $\gamma \approx R_\rho^\star/Le$ being too crude far from onset. A quick look at figure 9(*b*) indeed reveals that another limit assuming a constant value of γ instead could likely perform better on increasing $\epsilon^\star$.

Using the power balance (3.34) combined with (C3) allows us to derive the corresponding scaling for Pe

$$Pe \sim |Ra_T|^{1/4} \epsilon^{\star \alpha_1/2 + 1/4} Pr^{\alpha_1/4} Le^{1-\alpha_1/2} \approx |Ra_T|^{1/4} \epsilon^{\star 0.95} Pr^{0.17} Le^{0.30}, \qquad \text{(C4)}$$

where $\alpha_1 = 1.4$ has been used.

Although we acknowledge the fact that figure 21 merely provides empirical fits to the data, it is worth stressing that the simple polynomial fits considered here provide a better agreement with the actual data than the weakly nonlinear theory derived in § 3.5.1.

REFERENCES

ASCHER, U.M., RUUTH, S.J. & SPITERI, R.J. 1997 Implicit-explicit Runge–Kutta methods for time-dependent partial differential equations. *Appl. Numer. Maths* **25** (2–3), 151–167.

BACKUS, G.E., PARKER, R. & CONSTABLE, C.G. 1996 *Foundations of Geomagnetism*. Cambridge University Press.

BAINES, P.G. & GILL, A.E. 1969 On thermohaline convection with linear gradients. *J. Fluid Mech.* **37** (2), 289–306.

BELMONTE, A., TILGNER, A. & LIBCHABER, A. 1994 Temperature and velocity boundary layers in turbulent convection. *Phys. Rev.* E **50** (1), 269–279.

BOSCARINO, S., PARESCHI, L. & RUSSO, G. 2013 Implicit-explicit Runge–Kutta schemes for hyperbolic systems and kinetic equations in the diffusion limit. *SIAM J. Sci. Comput.* **35** (1), A22–A51.

BOYD, J.P. 2001 *Chebyshev and Fourier Spectral Methods: Second Revised Edition*. Courier Corporation.

BREUER, M., MANGLIK, A., WICHT, J., TRÜMPER, T., HARDER, H. & HANSEN, U. 2010 Thermochemically driven convection in a rotating spherical shell. *Geophys. J. Intl* **183**, 150–162.

BROWN, J.M., GARAUD, P. & STELLMACH, S. 2013 Chemical transport and spontaneous layer formation in fingering convection in astrophysics. *Astrophys. J.* **768** (1), 34.

CHRISTENSEN, U.R. & AUBERT, J. 2006 Scaling properties of convection-driven dynamos in rotating spherical shells and application to planetary magnetic fields. *Geophys. J. Intl* **166**, 97–114.

CHRISTENSEN, U.R. & WICHT, J. 2015 Numerical dynamo simulations. In *Treatise on Geophysics* (ed. P. Olson), 2nd edn, vol. 8: Core Dynamics, pp. 245–282. Elsevier.

DESCHAMPS, F., TACKLEY, P.J. & NAKAGAWA, T. 2010 Temperature and heat flux scalings for isoviscous thermal convection in spherical geometry. *Geophys. J. Intl* **182**, 137–154.

GARAUD, P. 2018 Double-diffusive convection at low Prandtl number. *Annu. Rev. Fluid Mech.* **50** (1), 275–298.

GARAUD, P. & BRUMMELL, N. 2015 2D or not 2D: the effect of dimensionality on the dynamics of fingering convection at low Prandtl number. *Astrophys. J.* **815** (1), 42.

GARAUD, P., MEDRANO, M., BROWN, J.M., MANKOVICH, C. & MOORE, K. 2015 Excitation of gravity waves by fingering convection, and the formation of compositional staircases in stellar interiors. *Astrophys. J.* **808** (1), 89.

GASTINE, T., WICHT, J. & AURNOU, J.M. 2015 Turbulent Rayleigh–Bénard convection in spherical shells. *J. Fluid Mech.* **778**, 721–764.

GLATZMAIER, G.A. 1984 Numerical simulations of stellar convective dynamos. I – the model and method. *J. Comput. Phys.* **55**, 461–484.

GOLUSKIN, D., JOHNSTON, H., FLIERL, G.R. & SPIEGEL, E.A. 2014 Convectively driven shear and decreased heat flux. *J. Fluid Mech.* **759**, 360–385.

GROSSMANN, S. & LOHSE, D. 2000 Scaling in thermal convection: a unifying theory. *J. Fluid Mech.* **407**, 27–56.

GUERVILLY, C. 2022 Fingering convection in the stably stratified layers of planetary cores. *J. Geophys. Res.: Planet.* **127** (11), e2022JE007350.

HAGE, E. & TILGNER, A. 2010 High Rayleigh number convection with double diffusive fingers. *Phys. Fluids* **22** (7), 076603.

HAUCK, S.A., DOMBARD, A.J., PHILLIPS, R.J. & SOLOMON, S.C. 2004 Internal and tectonic evolution of Mercury. *Earth Planet. Sci. Lett.* **222** (3), 713–728.

HOLYER, J.Y. 1984 The stability of long, steady, two-dimensional salt fingers. *J. Fluid Mech.* **147**, 169–185.

HUNTER, J.D. 2007 Matplotlib: a 2D graphics environment. *Comput. Sci. Engng* **9** (3), 90–95.

JARVIS, G.T. 1993 Effects of curvature on two-dimensional models of mantle convection – cylindrical polar coordinates. *J. Geophys. Res.* **98**, 4477–4485.

JULIEN, K., RUBIO, A.M., GROOMS, I. & KNOBLOCH, E. 2012 Statistical and physical balances in low Rossby number Rayleigh–Bénard convection. *Geophys. Astrophys. Fluid Dyn.* **106** (4–5), 392–428.

KING, E.M., STELLMACH, S. & AURNOU, J.M. 2012 Heat transfer by rapidly rotating Rayleigh–Bénard convection. *J. Fluid Mech.* **691**, 568–582.

KUNZE, E. 1987 Limits on growing, finite-length salt fingers: a Richardson number constraint. *J. Mar. Res.* **45** (3), 533–556.

LABROSSE, S. 2015 Thermal evolution of the core with a high thermal conductivity. *Phys. Earth Planet. Inter.* **247**, 36–55.

LAGO, R., GASTINE, T., DANNERT, T., RAMPP, M. & WICHT, J. 2021 MagIC v5.10: a two-dimensional message-passing interface (MPI) distribution for pseudo-spectral magnetohydrodynamics simulations in spherical geometry. *Geosci. Model Develop.* **14** (12), 7477–7495.

LIU, C., JULIEN, K. & KNOBLOCH, E. 2022 Staircase solutions and stability in vertically confined salt-finger convection. *J. Fluid Mech.* **952**, A4.

LONG, R.S., MOUND, J.E., DAVIES, C.J. & TOBIAS, S.M. 2020 Thermal boundary layer structure in convection with and without rotation. *Phys. Rev. Fluids* **5** (11), 113502.

MALKUS, W.V.R. 1954 The heat transport and spectrum of thermal turbulence. *Proc. R. Soc. Lond.* A **225** (1161), 196–212.

MANKOVICH, C.R. & FORTNEY, J.J. 2020 Evidence for a dichotomy in the interior structures of Jupiter and Saturn from helium phase separation. *Astrophys. J.* **889** (1), 51.

MONVILLE, R., VIDAL, J., CÉBRON, D. & SCHAEFFER, N. 2019 Rotating convection in stably-stratified planetary cores. *Geophys. J. Intl* **219** (Supplement_1), S195–S218.

OHTA, K., KUWAYAMA, Y., HIROSE, K., SHIMIZU, K. & OHISHI, Y. 2016 Experimental determination of the electrical resistivity of iron at Earth's core conditions. *Nature* **534** (7605), 95–98.

ORUBA, L. 2016 On the role of thermal boundary conditions in dynamo scaling laws. *Geophys. Astrophys. Fluid Dyn.* **110** (6), 529–545.

PAPARELLA, F. & SPIEGEL, E.A. 1999 Sheared salt fingers: instability in a truncated system. *Phys. Fluids* **11** (5), 1161–1168.

POZZO, M., DAVIES, C., GUBBINS, D. & ALFÈ, D. 2012 Thermal and electrical conductivity of iron at Earth's core conditions. *Nature* **485**, 355–358.

PRIESTLEY, C.H.B. 1954 Convection from a large horizontal surface. *Austral. J. Phys.* **7**, 176.

RADKO, T. 2003 A mechanism for layer formation in a double-diffusive fluid. *J. Fluid Mech.* **497**, 365–380.

RADKO, T. 2010 Equilibration of weakly nonlinear salt fingers. *J. Fluid Mech.* **645**, 121–143.

RADKO, T. 2013 *Double-Diffusive Convection*. Cambridge University Press.

RADKO, T. & SMITH, D.P. 2012 Equilibrium transport in double-diffusive convection. *J. Fluid Mech.* **692**, 5–27.

RADKO, T. & STERN, M.E. 2000 Finite-amplitude salt fingers in a vertically bounded layer. *J. Fluid Mech.* **425**, 133–160.

ROBERTS, P.H. & KING, E.M. 2013 On the genesis of the Earth's magnetism. *Rep. Prog. Phys.* **76**, 096801.

ROSENTHAL, A., LÜDEMANN, K. & TILGNER, A. 2022 Staircase formation in unstably stratified double diffusive finger convection. *Phys. Fluids* **34** (11), 116605.

SCHAEFFER, N. 2013 Efficient spherical harmonic transforms aimed at pseudospectral numerical simulations. *Geochem. Geophys. Geosyst.* **14** (3), 751–758.

SCHLICHTING, H. & GERSTEN, K. 2018 *Boundary-Layer Theory*, 9th edn. Springer.

SCHMITT, R.W. 1979*a* Flux measurements on salt fingers at an interface. *J. Mar. Res.* **37** (3), 419–436.

SCHMITT, R.W. 1979*b* The growth rate of super-critical salt fingers. *Deep-Sea Res.* **26** (1), 23–40.

SHEN, C.Y. 1995 Equilibrium salt-fingering convection. *Phys. Fluids* **7** (4), 706–717.

SILVA, L., MATHER, J.F. & SIMITEV, R.D. 2019 The onset of thermo-compositional convection in rotating spherical shells. *Geophys. Astrophys. Fluid Dyn.* **113** (4), 377–404.

SMYTH, W.D. & KIMURA, S. 2007 Instability and diapycnal momentum transport in a double-diffusive, stratified shear layer. *J. Phys. Oceanogr.* **37** (6), 1551–1565.

STELLMACH, S., TRAXLER, A., GARAUD, P., BRUMMELL, N. & RADKO, T. 2011 Dynamics of fingering convection. Part 2. The formation of thermohaline staircases. *J. Fluid Mech.* **677**, 554–571.

STERN, M.E. 1960 The "salt-fountain" and thermohaline convection. *Tellus* **12** (2), 172–175.

STERN, M.E. 1969 Collective instability of salt fingers. *J. Fluid Mech.* **35** (2), 209–218.

STERN, M.E. 1975 Thermohaline convection. In *Ocean Circulation Physics*, International Geophysics, vol. 19, chap. 11. Academic.

STERN, M.E. & RADKO, T. 1998 The salt finger amplitude in unbounded T-S gradient layers. *J. Mar. Res.* **56** (1), 157–196.

STERN, M.E. & SIMEONOV, J. 2005 The secondary instability of salt fingers. *J. Fluid Mech.* **533**, 361–380.

TAYLOR, J. & BUCENS, P. 1989 Laboratory experiments on the structure of salt fingers. *Deep-Sea Res.* **36** (11), 1675–1704.

TAYLOR, J. & VERONIS, G. 1996 Experiments on double-diffusive sugar–salt fingers at high stability ratio. *J. Fluid Mech.* **321**, 315–333.

THYNG, K., GREENE, C., HETLAND, R., ZIMMERLE, H. & DIMARCO, S. 2016 True colors of oceanography: guidelines for effective and accurate colormap selection. *Oceanography* **29** (3), 9–13.

TILGNER, A., BELMONTE, A. & LIBCHABER, A. 1993 Temperature and velocity profiles of turbulent convection in water. *Phys. Rev.* E **47** (4), R2253.

TRAXLER, A., GARAUD, P. & STELLMACH, S. 2011*a* Numerically determined transport laws for fingering (thermohaline) convection in astrophysics. *Astrophys. J.* **728** (2), L29.

TRAXLER, A., STELLMACH, S., GARAUD, P., RADKO, T. & BRUMMELL, N. 2011*b* Dynamics of fingering convection. Part 1. Small-scale fluxes and large-scale instabilities. *J. Fluid Mech.* **677**, 530–553.

TURNER, J.S. 1967 Salt fingers across a density interface. *Deep-Sea Res.* **14** (5), 599–611.

TURNER, J.S. 1973 *Buoyancy Effects in Fluids*. Cambridge University Press.

VALDETTARO, L., RIEUTORD, M., BRACONNIER, T. & FRAYSSÉ, V. 2007 Convergence and round-off errors in a two-dimensional eigenvalue problem using spectral methods and Arnoldi–Chebyshev algorithm. *J. Comput. Appl. Maths* **205** (1), 382–393.

VANGELOV, V.I. & JARVIS, G.T. 1994 Geometrical effects of curvature in axisymmetric spherical models of mantle convection. *J. Geophys. Res.* **99**, 9345–9358.

VERONIS, G. 1965 On finite amplitude instability in thermohaline convection. *J. Mar. Res.* **23** (1), 1–17.

WARDINSKI, I., AMIT, H., LANGLAIS, B. & THÉBAULT, E. 2021 The internal structure of Mercury's core inferred from magnetic observations. *J. Geophys. Res.: Planet.* **126** (12), e06792.

WICHT, J. 2002 Inner-core conductivity in numerical dynamo simulations. *Phys. Earth Planet. Inter.* **132** (4), 281–302.

XIE, J.-H., JULIEN, K. & KNOBLOCH, E. 2019 Jet formation in salt-finger convection: a modified Rayleigh–Bénard problem. *J. Fluid Mech.* **858**, 228–263.

XIE, J.-H., MIQUEL, B., JULIEN, K. & KNOBLOCH, E. 2017 A reduced model for salt-finger convection in the small diffusivity ratio limit. *Fluids* **2** (1), 6.

YANG, Y. 2020 Double diffusive convection in the finger regime for different Prandtl and Schmidt numbers. *Acta Mechanica Sin.* **36** (4), 797–804.

YANG, Y., CHEN, W., VERZICCO, R. & LOHSE, D. 2020 Multiple states and transport properties of double-diffusive convection turbulence. *Proc. Natl Acad. Sci. USA* **117** (26), 14676–14681.

YANG, Y., VAN DER POEL, E.P., OSTILLA-MÓNICO, R., SUN, C., VERZICCO, R., GROSSMANN, S. & LOHSE, D. 2015 Salinity transfer in bounded double diffusive convection. *J. Fluid Mech.* **768**, 476–491.

YANG, Y., VERZICCO, R. & LOHSE, D. 2016 Scaling laws and flow structures of double diffusive convection in the finger regime. *J. Fluid Mech.* **802**, 667–689.